Lawrence Berkeley National Laboratory
Lawrence Berkeley National Laboratory

Title
Radiation tests of the EMU spacesuit for the International Space Station using energetic protons

Permalink
https://escholarship.org/uc/item/2qn909xw

Authors
Zeitlin, C.
Heilbronn, L.
Miller, J.
et al.

Publication Date
2001-06-04

Peer reviewed

Radiation Tests of the EMU Spacesuit for the International Space Station Using Energetic Protons

C. Zeitlin, L. Heilbronn, J. Miller
Lawrence Berkeley National Laboratory, Berkeley, California   94720

M. Shavers
Johnson Space Center, Houston, Texas

Measurements using silicon detectors to characterize the radiation transmitted through the EMU spacesuit and a human phantom have been performed using 155 and 250 MeV proton beams at the Loma Linda University Medical Center (LLUMC). The beams simulate radiation encountered in space, where trapped protons having kinetic energies on the order of 100 MeV are copious. Protons with 100 MeV kinetic energy and above can penetrate many centimeters of water or other light materials, so that astronauts exposed to such energetic particles will receive doses to their internal organs. This dose can be enhanced or reduced by shielding – either from the spacesuit or the self-shielding of the body – but minimization of the risk depends on details of the incident particle flux (in particular the energy spectrum) and on the dose responses of the various critical organs. Data were taken to characterize the beams and to calibrate the detectors using the beam in a treatment room at the LLUMC proton facility, in preparation for an experiment with the same beams incident on detectors placed in a human phantom within the EMU suit. Nuclear interactions of high-energy protons in various materials produce a small flux of highly ionizing, low-energy secondary radiation. Secondaries are of interest for their biological effects, since they cause doses and especially dose-equivalents to increase relative to the values expected simply from ionization energy loss along the Bragg curve. Because many secondaries have very short ranges, they are best measured in passive track detectors such as CR-39. The silicon detector data presented here are intended to supplement the CR-39 data in regions where silicon has greater sensitivity, in particular the portion of the LET spectrum below 5 keV/μm. The results obtained in this study suggest that optimizing the radiation shielding properties of spacesuits is a formidable task. The näive assumption that adding mass can reduce risk is not supported by the data, which show that reducing the dose delivered at or near the skin by low-energy particles may increase the dose delivered by energetic particles to points deeper in the body.

1.   INTRODUCTION

To accurately estimate doses and dose-equivalents received during extravehicular activities outside the International Space Station (ISS), one must take into account the shielding properties of the spacesuits worn by the astronauts and the self-shielding of the human body with respect to critical areas such as the blood-forming organs and central nervous system. In the ISS orbit, there are large fluxes of both protons and electrons with sufficient kinetic energy to penetrate several millimeters of light materials such as fabric or tissue; these fluxes are largest in the trapped particle belts [1]. Although the proton spectrum falls off rapidly with increasing energy, there is a significant flux above 100 MeV, where ranges exceed 10 cm of water and increase rapidly with energy. Proton beams with energies from 60 to 250 MeV, produced at the Loma Linda University Medical Center (LLUMC) cancer treatment facility [2], were used in the measurements reported here.

Because the EMU spacesuit is complex and highly inhomogeneous, measurements are needed to definitively determine threshold energies for suit penetration and dose vs. depth relationships for various regions, including the skin and points well inside the body when enclosed by the spacesuit. Many parts of the suit have areal densities of only 0.2 g cm^{-2}, but even the thinnest parts will stop the large fluxes of very low-energy protons (E < 12 MeV) and electrons (E < 0.5 MeV) encountered in the trapped belts. Energy thresholds for suit penetration of electrons and protons were measured at the LLUMC with ionization chambers [3]; the data have been used as input to a computer model of the suit [4]. The threshold energies, while vitally important for understanding the shielding properties of various parts of the EMU suit against low-energy particles, are only part of the required data. It is also necessary to determine the effects of the spacesuit – and the tissue inside it – on the charged particles with sufficient energy to penetrate the suit and, at the higher energies, many centimeters of tissue.

When highly penetrating radiation (e.g., an energetic proton) traverses a significant depth of shielding and/or tissue, secondary particles produced in nuclear interactions are of concern. Highly ionizing secondaries can be produced in grazing interactions in which a target nucleus recoils, or in more central collisions where the target nucleus breaks apart, sometimes with additional emission of low-velocity charged particles from the decay of excited nuclear states in the abrasion-ablation process [5]. When one integrates fluence over the linear energy transfer (LET[1]) spectrum to obtain dose equivalent, secondary particles with high LET – though not numerous – get a large weighting from the quality factor [6], resulting in a significant contribution to dose equivalent [7].

Measurements of the short-ranged, high-LET secondaries produced by an incident beam can be made with CR-39 plastic nuclear track detectors, in combination with TLDs to measure the total dose in a particular exposure [8]. Low-energy particles from target recoils or fragmentation have short ranges, on the order of hundreds of microns or less in water or tissue; for instance, a ^{12}C nucleus with kinetic energy of 4 MeV/nucleon (about half the maximum possible recoil energy from a 250 MeV proton) has a range of about 85 μm in water, with an initial LET of about 340 keV/μm. Measuring the fluence and LET of such tracks presents many technical challenges; CR-39 is well-suited for this purpose but can only detect particles with LET above about 5 keV/μm, approximately an order of magnitude greater than the LET of the LLUMC 250 MeV proton beam. Thus, in the present experiment, the primary beam particles and any secondaries with LET below 5 keV/μm are missed by CR-39. Tracks with ranges shorter than about 10 μm in CR-39 are also missed; these include the tracks from very low-energy target fragments and recoil nuclei. These very short tracks are removed in the etching process [9]; they can have very high LET, and consequently contribute significantly to dose and dose equivalent.

The silicon detector system described here has more typically been used in the measurement of high-energy heavy ion beams and their nuclear fragmentation products [10-14]. Silicon detectors have some advantages compared to CR-39 in this experimental setting, particularly their ability to measure energy deposition events over a dynamic range large enough to include the primary protons and a broad spectrum of secondaries. However, the detectors used here have significant disadvantages in the measurement of short-ranged secondaries: (1) they have "dead layers" (typically about 2% of the detector depth), and (2) they collect charge in a huge volume (compared to CR-39), so that – as explained in more detail below – the direct measurement of the LET of short-ranged secondaries is impossible. However, since the high end of the LET spectrum can be reliably measured in CR-39, we focus on the lower end, and we attempt to find areas of overlap where the two measurement methods can be cross-checked for consistency.

2. EXPERIMENTAL CONFIGURATIONS

A. Detectors and Electronics

The accelerator at the LLUMC provided proton beams at energies similar to those encountered in the trapped particle belts through which the ISS will pass. Beams with kinetic energies of 250 MeV and 155 MeV at extraction from the synchrotron were made available for the present study and for the measurements of the EMU suit penetration energies. The 155 MeV beam was also used to produce beams with energies of about 60 and 40 MeV by passing the protons through blocks of plastic with the appropriate depths.

The measurements described here were done in January 2000 in Gantry 1, a room designed for patient treatment. Data were taken both with and without the EMU suit. To simulate a human body inside the EMU suit, the experiments used a phantom [15] consisting of large portions of a human skeleton and water-equivalent plastic. A frontal view of the phantom is shown in Fig. 1. Holes were drilled to allow experimenters to put detectors, encased in tissue-equivalent plastic, in various locations inside the phantom. The phantom is modular; pieces were taken as needed and placed inside the appropriate part of the EMU suit. Gantry 1 was a convenient location for these runs, as it has a motor-driven table that can be moved into the beam, and the beamline itself can be rotated around the table to accommodate a variety of entrance port requirements for treatment.

The first set of measurements used only the bare beam at the four energies mentioned above; these data allow us to calibrate our silicon detector system and to characterize both the beam and the response of the detectors to it. A second set

---

[1] Throughout, we use "LET" as shorthand meaning LET$_\infty$ in water.

of measurements was taken with the same detectors placed inside the phantom at three locations: brain, upper abdomen and lower abdomen. The phantom was placed inside the appropriate piece of the EMU suit for each location.

In all runs, a stack of three lithium-drifted silicon detectors was used. The detectors are right-circular cylinders, with radii of 1.2 cm and depths from 3.06 to 3.08 mm. They measure the deposited energy (ΔE) from the ionization energy losses of charged particles traversing their sensitive volumes. In the measurements with the bare beams in Gantry 1, detectors were placed in a housing typically used on an optical bench at an accelerator. Here, the housing was placed flat on the treatment table with the beam incident vertically from above, as shown schematically in Fig. 2(a). We refer to the detectors as d3mm1, d3mm2, and d3mm3, with d3mm1 being closest to the nozzle (the end of the beam transport vacuum line). A sketch of the arrangement of detectors and water-equivalent plastic plugs used in the spacesuit/phantom runs is shown in Fig. 2(b).

The detectors were biased to full depletion. The charge liberated in each detector was integrated and amplified by a charge-sensitive preamplifier and shaping amplifier combination, the Amptek A225 [16], chosen for its very low noise and compactness (a major issue given the limited space in Gantry 1). Each A225 has two outputs, a fast signal used for timing and triggering, and a slow shaped signal (rise time ~ 2 μsec) for precise determination of pulse height. The shaped outputs were further amplified by Tennelec Model 222 biased amplifiers; those outputs were connected to 50' BNC cables, which ran from the gantry to the hallway just outside, where NIM logic modules and a CAMAC crate were located; the signals were digitized in a 12-bit, peak-sensing CAMAC ADC.

The fast signal from d3mm1 was used as input to a constant-fraction discriminator (CFD), the output of which was used to trigger the readout. If a second fast signal arrived during the ≈ 30 μsec readout time of the previous event, the second trigger was vetoed. The ADC was gated on for 5 μsec by a signal derived from the CFD output; a second event arriving within this window can, in some cases, distort the pulses and cause spuriously large ADC readings, as discussed in more detail below. The ADC results were read out by a Vax computer and the events stored on disk in an event-by-event format.

B. Calibration

In silicon, one electron/hole pair is created for each 3.6 eV of energy deposited; the observed pulse heights were converted to deposited energy (ΔE) using the following procedure to calibrate each channel from preamplifier through ADC. An EG&G Ortec 447 Research Pulser supplied a series of voltage pulses with accurately known amplitude to a reference capacitor, yielding a charge that was injected directly into the preamp on the same path as the charge coming from the detector. Calibration data were acquired and stored on disk in the same way as beam data; off-line, the data were analyzed to determine the slope and pedestal for each channel. As is typical for these amplifiers and ADCs, excellent linearity is seen over the relevant range of ΔE.

C. Relation of ΔE in Silicon to LET

Energy loss in silicon detectors can be related to energy loss in water. Calculations using the Bethe-Bloch equation [17] show that, for the range of energies encountered in these experiments, it is reasonable to relate measured deposited energy ΔE in silicon to LET using a single conversion constant. To a good approximation, LET = 0.53 · (ΔE/Δx) where Δx is the sensitive depth of the silicon. However, when we discuss target fragmentation or target recoil events, it is important to bear in mind that the detectors record the total energy deposited, regardless of the length of a track in the detector. Converting ΔE to LET as per the preceding equation is, by definition, averaging over the entire depth of the detector; this can be orders of magnitude greater than the range of a high-LET track. In such cases, the conversion of ΔE to LET is not meaningful. Only for particles that pass entirely through a detector, parallel or nearly parallel to the nominal beam axis, can one accurately relate ΔE to LET. For stopping particles, estimates of LET obtained from ΔE/Δx are lower limits.

Preliminary model calculations[2] indicate that the LET spectrum of target fragments produced in proton-silicon interactions is quite complex, and contains a non-negligible fluence of events out to several thousand keV/μm. Most of

---

[2] A model of proton-silicon interactions is under development as we wish to study the physical processes that underlie the measured ΔE distributions. It will be extended to proton-carbon and proton-proton interactions, with the goal of modeling target fragment production in tissue.

the details of this spectrum are impossible to measure in the present experimental configuration. Even in CR-39, significant details of the target fragment spectrum may be lost, since the ranges of the target fragments and recoiling target nuclei are extremely short – above 500 keV/μm, most tracks have ranges in water of less than 5 μm.

3. ANALYSIS OF BARE-BEAM DATA

The first runs in Gantry 1 used the proton beam at two values of extracted energy, 250 and 155 MeV, and two additional values of nozzle energy (the energy of the beam as it enters the air gap between the end of the beam line and the detectors). The two lower energies – nominally 60 and 40 MeV – were obtained by passing the 155 MeV beam through thick (> 10 cm water-equivalent) plastic range shifter blocks placed at the end of the vacuum line. Neither the EMU suit nor the phantom were used in these runs.

A. Beam Quality

The Gantry 1 facility is primarily used for patient treatment, with typical intensities of 10^8 protons s^{-1} cm^{-2} and higher; our experiment requires a beam intensity of 10^3 protons s^{-1} cm^{-2} or lower. This disparity presented a number of difficulties to the accelerator operator, whose feedback and monitoring devices did not register such small beam currents. As a result, currents were slightly higher than optimal, and some event pile-up (described below) occurred. Because beam intensity varied from run to run, so did the fraction of pile-up events. The treatment of these events is the leading source of systematic error in the data analysis.

The beam spot at the treatment table was considerably larger than the 1.2 cm radius of the detectors. The beams have considerable divergence, caused by two factors: (1) the beam transport optics, which focus the beam at a point upstream of the nozzle, and (2) scattering foils also placed far upstream of the nozzle. Focusing with quadrupole magnets produces a small, divergent beam spot that is enlarged and made more uniform by the scattering foils. Because Coulomb multiple scattering increases with decreasing energy, a set of thinner scattering foils is required to produce the desired spot size with the 155 MeV beam than with the 250 MeV beam. As we will show, the divergence of the beam has noticeable effects on the spectra seen in the silicon detectors.

B. ΔE Spectra: Events Lost By Scattering

The ΔE spectra for the 250 MeV bare-beam run are shown in the histograms in Fig. 3(a), (b), and (c), for detectors d3mm1, 2, and 3 respectively. The only cut applied in these three histograms is the requirement[3] that ΔE in d3mm1 was above 1.4 MeV. Peaks appear near the expected ΔE values, with tails of events to higher ΔE. A small peak of events in each plot appears in the highest ΔE bin; these are events where a relatively large signal saturated the readout electronics. In all three of the histograms in Fig. 3(a)-(c), about 0.28% of events appear in this "overflow" bin. Also, d3mm2 (about 2%) and d3mm3 (about 5%) have considerable numbers of events with ΔE near 0; these are likely events in which the incident proton hit near the edge of d3mm1 and had a trajectory with a sufficiently large angle with respect to the beam axis that it missed the active area of d3mm2 and/or d3mm3. Our beamline simulation model [14] reproduces these fractions with reasonable accuracy, predicting 1.8% losses in d3mm2 and 7.5% losses in d3mm3. The model shows that Coulomb scattering in the beam-spreading foils is the primary cause of events in which protons hit d3mm1 but miss d3mm2 and/or d3mm3.

C. Event Pile-up in the ΔE Spectra

In the d3mm1 spectrum, Fig. 3(a), a peak is visible just above 4 MeV, close to double the ΔE of the main peak. This second peak, which sits on top of the high-end tail of the single-proton distribution, is due to pile-up events with two protons. These can also be identified in scatter plots of ΔE in any pair of detectors; Fig. 4(a) shows an example, with ΔE in d3mm2 plotted against ΔE in d3mm1 for the same event sample as in Fig. 3(a)-(c). Events in which both detectors were hit by the same particle or particles give well-correlated values of ΔE, and these heavily populate the region along a

---

[3] This value of ΔE was obtained from a Gaussian fit to the central bins of the proton peak in the d3mm1 spectrum. A ΔE of 1.4 MeV is to 3 standard deviations (3σ) below the mean of the peak found by the fit.

line drawn from the origin at 45º. Bands of events with relatively large ΔE in one detector or the other (but not both) are visible. If we take a projection of the entire sample onto either axis, the number of events above the nominal proton ΔE will be greatly enhanced by the events along the 45º line with ΔE above about 4 MeV in each detector. In Fig. 4(b), we show the same events, restricted to the region below about 12 MeV, as a contour plot with logarithmic sensitivity. The contours indicate a strong concentration of events with hits corresponding to one proton in both d3mm1 and d3mm2. The other contours contain events where d3mm2 was missed (ΔE near 0), as well as pile-up events and possible good events (with only one incident proton) in which both detectors legitimately record a large ΔE due to relatively high-energy secondaries with sufficient range to register a signal in each. There is, in this plot, an unmistakable concentration of events in which both detectors record ΔE about twice that of a single proton; these are dominated by pile-up.

In the subsequent analysis, we use four methods to deal with pile-up events. The methods are as follows: (1) A graphical cut to exclude events in regions likely to be dominated by pile-up, as illustrated by the cut contour shown in Fig. 4(a) and more clearly in 4(b). (2) A cut to require that the ΔE in d3mm1 was within a narrow range centered on the proton peak, and then examine the spectra of events passing the cut in d3mm2 and d3mm3. (3) A cut to require that ΔE in d3mm2 is in the proton peak, and examine the spectra of events passing the cut in d3mm1 and d3mm3. (4) No cut, and look only at the ΔE range well above any likely pile-up events. For example, given a proton peak at 2.5 MeV, we might choose to examine the spectrum above 7.5 or 10 MeV, corresponding to ΔE greater than three or four times that of a single proton. This is the least biased of the methods since no cuts are made. As long as there is not a large contamination of pile-up events in a sample, this should yield the most reliable results, although it biases against legitimate high-ΔE events with ΔE below the cutoff.

A cut requiring ΔE greater than four times the value of single protons allows us to include any He fragments that are likely to be produced. If it were possible to produce ^{4}He at the beam velocity, any such fragments would have an initial dE/dx four times greater than that of a proton. Naively, we do not expect any He fragments to have the full beam velocity, based simply on invoking momentum conservation in the "brick wall" approximation. If, for example, a 223 MeV proton transfers twice its momentum (the maximum possible in this picture) to a ^{4}He fragment – and none to the other nucleons in the target nucleus – then the fragment would have a velocity only slightly more than half that of the incident proton[4]. It would accordingly have an initial dE/dx about twelve times that of the proton, far above the cut.

D. High-ΔE Tails, Pile-up Removal Methods

In the following, we use the 250 MeV and 155 MeV data sets. The spectra obtained with the lower-energy protons are strongly affected by the range-shifting blocks placed on the beamline; energy-loss straggling in the blocks leads to very broad distributions of the proton energy at the exit from the beam transport line. We are interested here in the high-ΔE tails of the distributions in the detectors, and the broad incident energy distributions render these data unsuitable for this purpose. The main use for the low-energy data is in fine-tuning the pulse-height-to-energy-loss calibration (see sub-section *F* below).

Figure 5 shows a histogram of events in d3mm1 after a pile-up rejection cut of type (1) is applied. A small peak persists around 4 MeV, but it is greatly reduced compared to the pile-up peak in Fig. 3(a). Because we have presumably removed the vast majority of pile-up events, we can make a somewhat loose operational definition of high-ΔE events as being those with $\Delta E > 2 \, \Delta E_{peak}$, where ΔE_{peak} is defined as the mean obtained from fitting a Gaussian to the central bins of the single-proton peak (the fitted curve is shown in the figure). In Fig. 5, about 0.5% of the events meet this definition, which in this case means ΔE > 4.54 MeV; in contrast, in the distribution in Fig. 3(a), with no pile-up rejection cuts, the fraction of events with ΔE > 4.54 MeV is 2.9%. This clearly shows that most high-ΔE events are removed by the type (1) cut, but we cannot tell from this simple analysis whether (or how many) valid target-fragmentation or target-recoil events have also been removed.

Applying pile-up rejection method (1) to the ΔE histograms for d3mm2 and d3mm3, we find 0.7% and 1.1% of events with $\Delta E > 2 \, \Delta E_{peak}$. These fractions are consistent with the hypothesis that some of the target fragments that are formed upstream (e.g., in d3mm1) have enough energy to reach at least one of the subsequent detectors. This effect leads to a build-up of fragments as one looks deeper in the detector stack. Since the physical processes in other materials are

---

[4] This simple calculation does not account for possible increases in fragment velocities due to Fermi motion of the target nucleons.

analogous, we expect a similar buildup effect in tissue, bone, etc. When we apply method (2), the tight cut requiring a single proton in d3mm1, and again examine the spectra with $\Delta E > 2\Delta E_{peak}$, we find almost precisely the same fractions of high-ΔE events (0.7% and 1.1%) in d3mm2 and d3mm3.

Method (3) invokes a tight cut on ΔE in d3mm2 to require a single proton there; we make this cut and then examine the d3mm1 and d3mm3 spectra. We find that this removes even more events in the high-end tail of the d3mm1 distribution than did method (1): only 0.3% of events among those passing the cut are found to have $\Delta E > 2\Delta E_{peak}$. In contrast, the effect on the d3mm3 distribution is much less severe – 0.9% of events are found in the high-end tail of that spectrum, roughly consistent with the fraction as determined by previous methods. These results suggest two interpretations: first, that many of the target fragments are produced with considerable momentum along the beam direction, so that they penetrate into at least one additional detector downstream from the one in which they originated; second, it may be that many of the protons that interact in d3mm1 are sufficiently perturbed that they do not meet the selection criterion in d3mm2, either because they are slowed down (so that their ΔE in d3mm2 is larger than nominal) or because they scatter at large angles and miss d3mm2 entirely. Whatever the mechanism, it is clear that by requiring a single proton in d3mm2, we are systematically biasing against high-ΔE events in d3mm1.

Turning now to method (4) and examining the d3mm1 spectrum, if we sum events in Fig. 3(a) with ΔE above 10 MeV, we find about 0.7% of the events of the sample. This is also true of the sample shown in Fig. 5. This is because the pile-up events almost all yield ΔE below 10 MeV. Since the fraction of events defined as high-ΔE by this method (0.7%) is larger than the 0.5% found using method (1), we tentatively conclude that method (1) does, as hypothesized, remove a significant portion of the valid target fragments from the sample. Applying method (4) to the d3mm2 and d3mm3 spectra shows that, for both, the fraction of events above 10 MeV is about 0.8%, roughly consistent with the fractions obtained by other methods.

Similar analysis of events in the high-ΔE tails has been performed on the 155 MeV beam data. In all cases, the results obtained with the lower-energy beam are quite close to those obtained at higher energy. This fits well with our expectation (explained below) that nuclear interactions are responsible for the high-ΔE tails, and the reaction cross sections are not very sensitive to beam energy variations in this range. The results presented in this section are summarized in Table 1.

E. Interpretation of the High-ΔE Tails

It is notable that, regardless of the method chosen to remove pile-up events and to define the high-ΔE tails, all the estimates of the fractions of high-ΔE events are in the range 0.5% to 1.1% (aside from the 0.2 – 0.3% obtained when we introduce a systematic bias against high-ΔE events, in the case of method (3) applied to d3mm1). As we will show, the high-ΔE events that remain in each spectrum after pile-up removal can be entirely ascribed to the elastic and inelastic scattering cross sections for protons on silicon. One of the more important conclusions we can draw from this is that there were no high-LET particles coming from the accelerator. High-LET particles could conceivably be produced in the beam transport line by the beam scraping against various apertures. The absence of such particles suggest the beam's trajectory is usually well-controlled through the transport line.

We note that the maximum recoil energy of a silicon nucleus being hit by a 250 MeV proton is about 40 MeV, or about 1.5 MeV/nucleon, corresponding to a range of just under 5 μm in silicon. The saturation point of the electronics in this experiment was around 30 MeV for most detectors, but the presence of counts in the overflow bin suggests that some events do in fact give this maximum energy deposition.

F. Beam Energies, Calibration Adjustment

We momentarily digress to discuss the peaks of the distributions, rather than the tails. The peak locations can, with the aid of careful energy-loss calculations, yield accurate measurements of the incident beam energies and help us to refine the calibration of the detectors.

The 250 and 155 MeV beams are expected to have nozzle energies of about 223 and 136 MeV, respectively [18]. The differences between extracted and nozzle energies are due to ionization energy losses in traversing the scattering foils and beam monitoring hardware, which included ionization chambers and a secondary emission monitor, located near the end of the vacuum line. In the following, we rely on calculations performed using a careful numerical integration of the Bethe-Bloch equation to determine energy loss in various beamline elements. The greater depth of scattering foils needed to spread the 250 MeV beam accounts for the 27 MeV energy loss of that beam after extraction, compared to the 19 MeV lost by the lower-energy beam.

6

For each silicon detector, the average ΔE on events with a single proton is determined by fitting a Gaussian distribution to the central bins of the peak, as illustrated in Fig. 5. These values are shown for each detector in Table 2, which also shows the results of calculations that assume a dead layer thickness of 2% of detector depth. In the data obtained with 250 MeV extracted beam, all reported ΔE values are lower than the calculation predicts, with the ratios of calculated to measured ΔE equal to 1.06, 1.10, and 1.08 for d3mm1, d3mm2, and d3mm3 respectively. Setting aside the question of what causes the discrepancies, we make use of the information by taking the ratios of calculated to measured ΔE in the 223 MeV beam data as correction factors, and applying them to the measured ΔE's in the other bare-beam data sets (and to subsequent analysis of this run). The corrected values are as shown in Table 2 for all runs other than the one at 250 MeV.

For the 155 MeV beam with no range-shifting blocks on the beamline, we varied the nozzle energy in the calculation until the predicted ΔE's were in good agreement with the corrected data; best agreement was obtained with 145 MeV for the nozzle energy, rather than the expected value of 136 MeV. A detailed calculation shows that this is highly consistent with the absence of one of the two scattering foils usually used for this beam. Further evidence for this comes from looking at the fractions of events with no hit in d3mm2 and/or d3mm3; these are found to be 1.0% and 3.8%, respectively. This is significantly less than would be expected if both foils were present, which would give a scattering distribution similar to that in the 250 MeV data, where the fractions of lost events were 2% and 5% for d3mm2 and d3mm3 respectively.

For the two lower energies that used the 155 MeV extracted beam, the calculation was performed assuming that both scattering foils were in place; we varied the amount of water-equivalent material on the beamline until we again obtained good agreement with the data. Nozzle energies were found to be 60 and 41 MeV with 10.2 and 11.75 cm of water-equivalent material, consistent with the expected values of 60 and 40 MeV, respectively. The LET's in water corresponding to the four nozzle energies of the beams are about 0.42, 0.58, 1.07, and 1.49 keV/μm, respectively.

In the 41 MeV data, there is a large disparity between the calculated and measured values of ΔE in d3mm3. A calculation for a 41 MeV proton predicts a range in silicon of 8.5 mm (8.1 mm for a 40 MeV proton). These facts are related: the observed disparity arises because beam particles were stopping in d3mm3, and straggling effects produce a very broad distribution of ΔE, as shown in Fig. 6. The calculation that predicts a 19.4 MeV energy loss for protons in d3mm3 is overly simple in its treatment of stopping particles, in that it is assumed that the full energy of the particle at the entrance to d3mm3 will be recorded in the detector. The reality – as shown by Fig. 6 – is more complex. Atomic physics effects including charge screening and charge pick-up reduce the amount of ionization energy deposited in the medium[5]. In this context, the calculated value of 19.4 MeV should be regarded as an approximate upper limit to ΔE in d3mm3. The data distribution bears this out: despite a FWHM of about 10 MeV, it drops steeply above 20 MeV.

To test the consistency of the agreement between the data and the calculations (excluding d3mm3 in the 41 MeV data), we performed for each detector a linear regression between the measured and calculated ΔE's. The fits give correlation coefficients greater than 0.9998, with most residuals less than 1% of the calculated values. The regression coefficients are used to further correct the ΔE's (compounded with the factors obtained from the 250 MeV run) in the analysis of the data sets with the detectors in the spacesuit/phantom.

G. Landau Distribution Calculations

Figures 7(a) and 7(b) show the same data as in Fig. 5, but here we focus on the central bins of the single-proton peak. Even when we restrict the fit to the six peak bins, as in Fig. 7(a), it is obvious that the data do not obey a Gaussian statistical distribution. From Fig. 5, it is also obvious that the data distribution just above the single-proton peak contains many more events than the fit distribution can account for. For the detectors used here, the Landau distribution [19] is expected to describe the spectra more accurately. We therefore generated several simulated Landau distributions of ΔE for 223 MeV protons in a 3 mm thick silicon detector, using a Monte Carlo method; the nominal parameters as per Ref. 19 predict a distribution broader than that seen in the data, an effect previously seen in other measurements [20]. This can be seen in Fig. 7(b), where the Landau distribution with nominal parameters is superimposed on the data (which are shown as a shaded histogram). Reducing the smearing term by 25% yields a distribution that agrees well with the d3mm1 data

---

[5] These effects cause the dE/dx vs. momentum curve to turn over below $\beta\gamma \approx 0.05$ [17], rather than continuing to increase as $1/\beta^2$. The simple calculation used here assumes the curve continues upward indefinitely.

in the tail region between 3 and 4 MeV; this simulated distribution has a negligible fraction of events (0.02%) with ΔE above 4 MeV. This is evidence that the high-ΔE events seen in the data (after pile-up removal) are due to nuclear interactions. Even the distribution shown in Fig. 7(b), which is overly broad and shifted to slightly higher ΔE than the data, has a negligible fraction of events with ΔE greater than twice that of the peak.

H. Nuclear Interactions and High-ΔE Tails

The bare-beam data provide us with needed information about the detector response, not just in single-proton events, but in events where an interaction between an incident proton and a silicon nucleus produces a large ΔE in one or more detectors. Proton-silicon (p-Si) nuclear interactions are qualitatively similar to, e.g., p-C interactions in tissue or p-Ca interactions in bone, so we may gain insight into those biologically-interesting reactions by examining p-Si interactions. Further, when considering the high-ΔE events due to interactions of beam protons in the spacesuit and tissue-equivalent materials, the high-ΔE events due to interactions occurring within the detectors must be taken into account as a source of background. For these reasons, it is necessary to understand the high-ΔE tails observed in the bare-beam data.

As discussed in detail in the Appendix, we estimate the total cross section for proton-silicon reactions at these energies to be about 634 mb (374 mb inelastic, 260 mb elastic). We therefore expect a total of 0.96% of protons to interact in a 3 mm thick silicon detector, consistent with the fractions of events seen in the high-end tails of the ΔE distributions in the bare-beam data. Actually, most of the estimates that were shown in Table 1 are smaller than 1%, but a difference in this direction is not surprising in view of the fact that we systematically under-count the high-ΔE events in the data. (The extent to which this is true depends on how the pile-up events are handled.) There are at least two ways in which we under-count events in which there were interactions. First, some reactions will result in ΔE's above the proton peak but not far enough above to meet any of our *ad hoc* definitions of the high-ΔE tail; second, some events with interactions may be removed by pile-up rejection cuts, particularly when we employ the graphical-cut technique, method (1), or the d3mm2 cut, method (3). Both of these pile-up rejection methods are prone to removing events with relatively light target fragments, such as a knock-out H or He nucleus. As previously described, an energetic, forward-going fragment produced in one detector can register a signal in the next detector. Similarly, when material is placed in close proximity to the detectors, target fragments produced there may penetrate into two or perhaps all three detectors. These events would not pass the graphical cut illustrated in Fig. 4, nor would they pass a tight cut requiring a single proton in d3mm2.

I. Quantitative Effects of the High-ΔE Tails

Table 3 shows the mean and RMS values of the ΔE distributions obtained in the 250 and 155 MeV runs using the four pile-up rejection methods. In the table, we define the quantity $\delta\Delta E$, the difference (in percent) between the average ΔE of a distribution and the ΔE of the single-proton peak in the same distribution. It is apparent that the average ΔE's shift to higher values as a result of nuclear interactions in the detectors; the effect is particularly evident in the 250 MeV data. In view of the relatively small probability of nuclear interactions (about 1% per detector), the shifts are large, ranging from 6% to 9%, depending on which method of pile-up rejection is used in a particular data set. The values of $\delta\Delta E$ in the 155 MeV data are not as large as those at the higher energy, suggesting that (1) there could be a decrease in the reaction cross sections (this is not expected, as per the previous discussion), or (2), the reduced energy available to either cause fragmentation or recoil of the target nucleus results in smaller energy depositions and hence fewer detectable high-ΔE events. A combination of the two factors may be responsible for the observed effect.

The changes in average ΔE are a measure of the dose (in silicon) arising from p-Si nuclear interactions. We again emphasize the point that the present data do not allow for direct measurements of LET of the secondaries. Also, the volume of the silicon detectors does not correspond to any particular biological target of interest (as would, for instance, a TEPC at the appropriate gas pressure), nor do the density and composition of the detectors correspond to tissue. Nonetheless, because dose is by definition a measure of energy deposition per unit volume, and because the physical processes in tissue are expected to be analogous, we can interpret the ΔE's measured in silicon detectors as roughly representing dose to tissue. This is a more accurate statement in the analysis of the spacesuit/phantom data, where the high-end tails of the ΔE distributions are dominated by target fragments, recoils, and other slow particles created in the spacesuit, tissue-equivalent material, and bones in the phantom.

Because we do not measure the target fragment LET distributions, we cannot estimate quality factors or dose equivalents. Fortunately, those estimates have been reliably made in the same spacesuit/phantom locations (and a few

others) using CR-39 [7]. The silicon detector data can be used as a cross-check on the estimated dose increases attributed to target fragments in the CR-39 data.

4. RESULTS WITH THE EMU SPACESUIT AND PHANTOM

The second set of runs made use of the EMU suit, phantom, and water-equivalent plugs of material (this is the same material as in the phantom). A housing for the silicon detectors was made of the water-equivalent material ($\rho = 1.0$ g cm^{-3}), with 27 mm of it upstream of d3mm1, 22 mm between d3mm1 and 2, and an additional 22 mm between d3mm2 and 3. The housing was placed in three hole locations (skull, upper abdomen, and lower abdomen) within the phantom, which were encased in the appropriate portion of the EMU suit. At all locations, data were taken with the 250 MeV and 155 MeV nominal beam energies. The ranges of the lower-energy beams were not sufficient to penetrate the material in front of d3mm1, hence there was little reason to run with them. In the following, we present results from each of the three locations.

A. General Considerations

Ionization energy loss in materials interposed between the nozzle and the detectors slows the protons, shifting the locations of the proton peaks to higher ΔE. For a given beam energy, the differences in spectra between bare beam data and data taken with various pieces of the EMU/phantom combination[6] are due to the site-specific EMU material and the water-equivalent plastic that comprised the detector holder, including the plugs between detectors. Target fragments produced in interactions of protons with nuclei in the suit or plastic may deposit energy in the detectors; to determine the fraction of events with fragments originating outside the detectors, we must subtract the fraction of high-ΔE events due to interactions in the detectors.

Given the proximity of the water-equivalent material plugs to the detectors, it is reasonable to ask whether relatively high-energy delta electrons produced in the plastic can cause large energy depositions in the detectors. The maximum electron kinetic energy is given, to a good approximation, by $T_{max} = 2\, m_e\, \beta^2 \gamma^2 c^2 = 0.54$ MeV for the 223 MeV beam and 0.32 MeV for the 136 MeV beam (where we use the nominal beam energies at the nozzle). The practical ranges for these electrons are about 2 mm and just under 1 mm of water, respectively [21]. High-ΔE events as we have defined them are always above 4 MeV, so that at least 10 maximum-energy deltas, all produced very near the detectors, would be required to explain a high-ΔE event; numerical integration of equation (23.7) of Ref. [17] shows that, with a 223 MeV beam, the rate of production of delta electrons is less than 1 per centimeter in water with a low-end cut of 100 keV electron energy. We therefore expect little or no contamination of the high-ΔE event samples from this source.

There are important differences between the configuration here compared to the bare-beam runs considered in the preceding. First, we have shown that the bare-beam spectra in d3mm2 and d3mm3 were influenced by target fragments formed in the detector(s) upstream. But in the arrangement considered here, there was a substantial amount of material in between each pair of detectors, so that slow particles produced far upstream, either in a preceding detector or in the plastic, might not reach a particular detector. This restricts the number of events with correlated high-ΔE in two detectors to those in which a relatively high-energy target fragment was created. Second, target fragments/recoils may be formed in the plastic in front of a particular detector and would have no influence on the ΔE recorded in the previous detector. Third, the additional materials – even though they are low-Z – result in increased Coulomb multiple scattering and losses of particles in the downstream detectors (d3mm2 and d3mm3)[7]. Overall, therefore, we expect less correlation of ΔE between detectors in these data than in the bare-beam data.

B. Brain Location: 223 MeV Beam

In the first of the runs with the spacesuit and phantom, the detectors, plugs, and their holder (also made of water-equivalent plastic) were placed in the phantom's head. The arrangement of detectors and plugs is sketched in Fig. 2(b). The top-most piece of the phantom was temporarily removed to allow access to the hole that had been made in a location

---

[6] In these data, we cannot separate the effects due to the spacesuit from those due to the phantom and the water-equivalent plastic.
[7] By definition, there is no loss of particles in d3mm1, since its discriminated signal was used as the trigger.

corresponding approximately to the middle of the brain. After the detectors were placed in the hole, the top piece of the skull was replaced. The phantom's head was then placed on the Gantry 1 treatment table and the EMU helmet placed over the head. The beam was again incident vertically from above.

Figures 8(a)-8(c) show histograms of energy deposited in d3mm1, 2, and 3 for the run with the 250 MeV proton beam in this configuration. For each histogram, a single cut has been applied to the data, requiring $\Delta E > 1.4$ MeV in that particular detector, in order to eliminate events where the detector was missed or was hit at its edge, where the charge collection efficiency is much less than 100%. There is little evidence of pile-up in these histograms; in particular, d3mm1 shows no sign of a peak at double the nominal proton ΔE. Detector d3mm2 shows a possible shoulder at about twice the proton ΔE, and d3mm3 shows a small peak there; fitting a Gaussian to the d3mm3 peak suggests that the number of pile-up events is less than 1% of the total.

Compared to the bare-beam spectra, all detectors show substantial increases in the fractions of events with high ΔE, as can be seen by examining the fractions obtained by the four methods previously defined. The results are shown in Table 4; the fractions are directly comparable to those in Table 1 for the bare-beam runs at the same extracted beam energies. We include the results from method (3), even though that method is overly restrictive with respect to the high-ΔE tail in d3mm1.

A few interesting trends can be seen in the fractions shown in Table 4. Excluding the method (3) results, we see that d3mm1 registers more high-ΔE events than the other detectors. Given the uneven distribution of materials (the helmet and 27 mm of plastic directly in front of d3mm1, compared to 22 mm of plastic directly in front of d3mm2 or d3mm3), this suggests the formation of many high-LET particles with sufficient energy to reach, and perhaps traverse, d3mm1, but which stopped in d3mm1 or in the plastic between d3mm1 and d3mm2. The fact that d3mm2 and d3mm3 show hints of pile-up, while d3mm1 does not, supports this interpretation: the expected $\approx 1\%$ of pile-up events with ΔE near twice ΔE_{peak} do not show up as a distinct peak because they are swamped by events with target fragments (that fail to reach d3mm2 and d3mm3) that deposit similar amounts of energy.

It is clear from Table 4 that method (4) yields significantly lower estimates of events in the tails than are found by the other methods. Because of this, and because these data show little evidence of pile-up, we have implemented a modified version of method (4), which we call method (4'), where we relax the definition of the high-end tail to be those events with $\Delta E > 3\ \Delta E_{peak}$. The fractions obtained with this looser definition are in somewhat better agreement with the other methods.

The single-proton peaks in Fig. 8(a)-(c) are shifted to higher ΔE's than in the bare-beam run due to the materials in between the nozzle and the detectors; the amount of the shift is an indirect measurement of the total mass of those materials. Using our beamline energy-loss code, we find that the ΔE_{peak} values found in these data are highly consistent with a proton energy of 181 MeV incident on d3mm1, implying energy losses totaling about 42 MeV in the helmet, phantom skull, and first water-equivalent plug. A calculation of energy lost by a 223 MeV beam in water shows that the materials in front of d3mm1 were equivalent to approximately 9.5 cm of water.

Taking the ratio of average ΔE over the entire spectrum to ΔE of the single-proton peak shows (roughly speaking) the effect of high-LET particles on dose. Using the ratio effectively divides out the increases due to energy loss that shift the spectra to higher ΔE. For all three detectors, the increase in the average using method (4) is 22-25%. In the bare-beam runs, the comparable increases were 13-15% due to interactions of protons in silicon. If we divide out[8] the increases found in the bare-beam runs (e.g., for d3mm1, we take 1.24/1.14), we find net increases of 9%, 8%, and 9% for d3mm1, 2, and 3 respectively, in remarkably good agreement with the 7.6% dose increase obtained with CR-39 for the same beam and detector placement [7]. This slightly higher dose increase observed with the silicon detectors may be related to the fact that CR-39 misses target fragments with LET below 5 keV/μm, which appear to be numerous, judging by the number of events in which two or three silicon detectors simultaneously record relatively large ΔE.

Repeating the preceding calculations using method (1), we find increases of 11-20%, compared to 6-9% in the bare-beam run. Again dividing out the bare-beam results, we find net increases of 13%, 3%, and 8% for the three detectors. The d3mm2 increase seems anomalously small; this may have to do with the details of the cut contour (which is somewhat subjective) used in this method. The other methods also show increases in average ΔE's in this data set

---

[8] This is an *ad hoc* attempt to account for the part of the dose increase (relative to the proton peak) that is due to the nuclear interactions that are known to occur in the detector, as per the preceding section.

compared to the bare-beam run. Method (2), which employs a tight cut on d3mm1, yields net increases of 2% and 6% for d3mm2 and d3mm3, respectively (note that d3mm2 again shows a very small increase); and method (3) (tight cut on d3mm2) yields net increases of 4% and 7% for d3mm1 and d3mm3, respectively. Recall that method (3) biases against high-ΔE in d3mm1. For d3mm3, the increases found by all methods are remarkably consistent, in all cases between 7% and 9%. The d3mm1 net increases are comparable, 9% and 13% using the least biased methods. The d3mm2 results do not agree particularly well with those from the other detectors except using method (4). The average ΔE's obtained by the various methods are summarized in Table 5.

In summary, we find a significant increase in the number of high-LET particles in this run compared to the bare-beam run at the same extracted energy. This increase correlates with increased average ΔE in the detectors, typically around 8-9% after accounting for p-Si interactions. This is quite similar to the 7.6% dose increase attributed to target fragments in the corresponding measurement using CR-39.

C. Brain Location: 136 MeV Beam

With the beamline configuration kept constant, the energy of the proton beam in the accelerator was changed to 155 MeV (extracted) and data-taking resumed. The spectra obtained in this run are shown in Fig. 8(d)-(f). The materials along the beam's path slowed the protons so that they stopped in the plastic between d3mm2 and d3mm3; this is why the d3mm3 spectrum has very nearly 100% of its entries at 0, and also explains the very broad distribution in d3mm2 (due to straggling near the end of the range).

We have applied the usual methods to obtain the fractions of events in the high-end tails for d3mm1 and d3mm2; the results are shown in the right half of Table 4. Relative to the 155 MeV bare-beam run, an increase in high-ΔE events in d3mm1 is seen, though it is not as large as in the higher-energy run at the same location (e.g., 3.2% in the tail using method (1) at this energy compared to 4.6% at the higher energy). It is obvious from Fig. 8(e) that we have little information about d3mm2 in regard to the high-ΔE tail, and we quote only upper limits for methods (4) and (4'). For the other methods, we find fewer high-end events in d3mm2 than in the comparable bare-beam data (right side of Table 1), likely due to the extremely low energy of the protons as they enter the plug in front of d3mm2 (at about 30 MeV) and as they exit the plug and enter d3mm2 (at about 17 MeV). There is simply not sufficient energy to produce (in the plug) many forward-going fragments with enough range to reach d3mm2; nor is there much energy available for p-Si interactions when the protons reach the detector. The decrease (relative to the 223 MeV beam) seen in the fraction of high-ΔE events in d3mm1 is qualitatively consistent with this picture (lower energy → fewer target fragments).

The ΔE$_{peak}$ values found in this run are found to be most consistent with calculations where the proton energy incident on d3mm1 is 66 to 67 MeV. In the previous section, we estimated from the 223 MeV beam data that the material in front of d3mm1 in this location represented about 9.5 cm of water; using a nozzle energy of 136 MeV, we predict an incident energy on d3mm1 of 68 MeV, in good agreement with the numbers obtained from the data. The agreement is slightly better with 9.6 cm of water-equivalent material in front of d3mm1 in the calculation.

Net dose increases as estimated (as in the preceding section) by dividing $\delta\Delta$E *in situ* by the corresponding $\delta\Delta$E in the bare-beam runs yields the following: Method (1), 5% increases in both d3mm1 and 2; method (2), a 10% increase in d3mm2; method (3), a 3% increase in d3mm1 (recall that this method is biased and yields very low estimates for d3mm1); and method (4), 2% increases in both d3mm1 and 2. Although there is some spread in these results, they are with one exception in the range 2 – 5%, and smaller than the corresponding net dose increases found in the same location with the 223 MeV beam.

D. Slice 8: 223 MeV Beam

The detectors were removed from the phantom's skull and placed inside the hole in slice 8 of the phantom, in the upper abdominal area as indicated in Fig. 1. The phantom's torso was placed inside the EMU suit's upper section and set on the treatment table with the detectors centered in the beam. The two parts of the buckle for the LCVG (liquid-cooled ventilation garment) inside the spacesuit were mated. It was noted that some of the detector area was shadowed by the buckle. The chemical composition and density of the buckle are not known to us at present, but it is metallic and not more than 3 cm thick. It was also noted that the suit's "swivel bearing," another metallic piece that rings the suit, was not directly between the nozzle and the detectors, but was not far from the beam, which has a diameter of 15–20 cm.

Figures 9(a)–9(c) are the ΔE histograms in d3mm1-3 obtained in this configuration with the 223 MeV beam. All three histograms show pronounced increases in the fractions of events above the proton peaks. The results obtained with the different pile-up rejection methods are shown in Table 6; they are typically in the 10-20% range, far larger fractions than

were seen in the brain data. The average ΔE's (see Table 7) are shifted to values that are more than double those of the proton peaks, a radical departure from the previous data sets. This is far in excess of any plausible increase from nuclear interactions; there is some other physical effect related to this placement of detectors that was not present in the data sets previously discussed.

The proton peak locations are most consistent with calculations where the proton energy incident on d3mm1 was about 205 MeV, with an estimated uncertainty of ±5 MeV; this is higher than the 181 MeV found with the same beam in the phantom's brain, meaning that there is – for the most part – less material between the nozzle and d3mm1 in this configuration. A separate calculation shows that the observed 18 MeV energy loss of the beam between the nozzle and d3mm1 would be produced by about 4.5 cm of water, 2.7 cm of which is accounted for by the first water-equivalent plug. The total of 4.5 cm is less than half of the 9.5 cm found to have been present upstream of d3mm1 in the measurement in the brain. It would therefore seem highly unlikely that the drastic increases in the fractions of events in the high-ΔE tails can be due to target fragments or recoils, given that there is less material for the protons to interact with.

Additional insight into the nature of the high-ΔE tails can be gained by examining the scatter plot of d3mm2 vs. d3mm1, shown in Fig. 10(a). The same data are shown as contours in Fig. 10(b). There is a high concentration of events with a single proton in the main peak of both detectors, visible as the small contours centered on about 2.5 MeV ΔE in each detector. Contours going towards higher ΔE in both detectors but especially in d3mm2 can be seen. The same data points make a nearly-vertical dark band of events in Fig 10(a). (The band is closer to vertical in 10a because of the greater range of ΔE in d3mm1 covered in this plot compared to 10(b).) This upward-turned band is due to protons that were slowed considerably from beam velocity before reaching d3mm1. Their velocities – already low before d3mm1 – are further reduced by the additional material between d3mm1 and d3mm2. Many of these protons will stop after d3mm2 and leave no signal in d3mm3; this is confirmed by noticing that in the d3mm3 histogram shown in Fig. 9(c), there are only 60% as many events with a hit above zero in d3mm3 as there are in Fig. 9(a), the corresponding histogram for d3mm1. Our beamline energy loss calculation shows that protons with energies below about 84 MeV will leave this type of ΔE pattern. We have calculated the correlation between ΔE in d3mm2 and ΔE in d3mm1 for slow protons, with incident energies on d3mm1 in the range from 55 to 120 MeV (corresponding to 80 – 135 MeV incident on the water-equivalent plug directly in front of d3mm1). The results of the calculation are shown in Fig. 10(c): the sharply-rising, nearly-vertical band seen in the data is accurately reproduced[9]. We conclude that these data contain many protons that have energies below 100 MeV when they reach d3mm1. To decrease a proton's energy from the 223 MeV nozzle energy to 100 MeV requires $24 - 40$ g cm^{-2} of material[10]; the first water-equivalent plug accounts for 2.7 g cm^{-2}, a small fraction of the total.

It is important to note that the scatter plots show no enhancement in the number of events that would correspond to two protons in each detector. We would expect some hint of this, particularly in the contours of Fig. 10(b), in the vicinity of $\Delta E = 5$ MeV in each detector, if there were significant pile-up in this data set. However, no enhancement is seen, consistent with the observation from the ΔE histograms that there appears to be very little pile-up in this run, or at least that the pile-up events are far outnumbered by the slow protons.

One conceivable explanation for the large number of high-ΔE events is that the LCVG buckle is responsible. It is possible that the slow protons seen in the detectors (especially in d3mm1) have scattered in from the buckle, and that they are slow because of ionization energy losses there. However, as we will show, if this is so, the buckle must have very high density in order to produce the observed proton energies. An alternative explanation is that some part of the beam was scraping an aperture in the transport line (see sub-section H below).

Computed tomography (CT) scans of the spacesuit/phantom, as shown in Fig. 11, show that only a small portion of the detector area was occluded by the buckle. It can also be seen that the buckle's long axis was not at 90° with respect to the beam direction; that is, protons passing through the buckle had to traverse a pathlength L, given by $L = d / \cos(\theta)$ where d is the depth of material and θ is the buckle's angle of inclination with respect to the normal to the beam axis. Using the MRI images, we estimate $\theta \approx 22°$. The outline of the plug that held the detectors is faintly visible as an outline,

---

[9] This is a highly abnormal correlation plot compared to that usually seen for two adjacent detectors; we emphasize that the presence of the 22 mm thick plug between the detectors is the cause.

[10] The areal density required is strongly dependent on the material's electron density. This amount of energy loss occurs in 24 g cm^{-2} of H_2O, 30 g cm^{-2} of Al, 34 g cm^{-2} of stainless steel, or 47 g cm^{-2} of Pb.

due to small air gaps around the edges; using this as a landmark to set the approximate scale of the image, we estimate that the buckle is 2.55 cm deep. Given its tilt with respect to the beam axis, this yields a pathlength of about 2.75 cm for particles going entirely through it. To facilitate visualizing the relative positions, in Fig. 11c we overlay a sketch of the detectors, along with a solid gray rectangle representing the detector holder. (The contrast of the buckle has been enhanced.) The sizes and positions of the detectors are roughly to scale. The full three-dimensional geometry is much more complicated than this single slice can represent; still, it is clear that most protons incident on d3mm1 missed the buckle entirely, and many others traversed only the corner of the buckle and therefore not the full depth. Few if any straight-line trajectories traverse the full depth of the buckle and hit the silicon detectors.

Assuming for the moment that the buckle is the source of the low-energy protons, we can get a rough estimate of its density. We hypothesize that the buckle is made of stainless steel, which has a density of 7.93 g cm^{-2}. Combined with the 2.55 cm depth estimate and the tilt angle, this yields an areal density of 21.8 g cm^{-2}, somewhat lower than the estimates above based on the proton energies seen in the data. Previously, we calculated that the maximum-energy protons (those missing the buckle) which hit d3mm1 had traversed about 4.5 cm of water-equivalent material, 2.7 cm of which is accounted for by the first plastic plug. This leaves about 1.8 g cm^{-2} for the other materials between the nozzle and the first plug, assuming those materials have electron densities similar to H_2O. A 223 MeV proton passing through this material and a 2.75 cm long path through the buckle would have an energy of 142 MeV at the first plug, and 122 MeV at d3mm1. There are certainly protons of this energy, and lower, incident on d3mm1 in the data. The presence of the lower-energy protons suggests that the actual density of the buckle is higher than that of stainless steel. If in fact the buckle is a comparatively low-density material, such as aluminum, then it cannot possibly be the source of the slow protons. In that case, it would have to have been that there was some other thick, dense piece of the spacesuit in the path of the beam during this run.

If the buckle has such high density, this would be consistent with the hypothesis that many slow protons in d3mm1 have initial trajectories several cm away from the beam centerline that undergo large deflections in the buckle from Coulomb multiple scattering. In this process, the RMS scattering angle is proportional to the charge Z of the material being traversed, and inversely proportional to the momentum of the incident particle. Thus a thick piece of dense, high-Z material will cause both significant energy loss and scattering, and the effects enhance one another – more scattering as momentum decreases leads to longer paths through the material, which in turn leads to still more scattering. For the case described just above, the average energy in the buckle (assumed to be stainless steel) is about 180 MeV; the calculated RMS scattering angle in steel is about 4.5° at this energy. Assuming a Gaussian[11] scattering distribution, this means that about 5% of the protons hitting the buckle have scattering angles of 9° or larger. A denser and higher-Z material than stainless steel would produce an even broader distribution, both because of increased scattering and increased energy loss; conversely, a less dense, lower-Z material such as aluminum would cause much less scattering – less than 2° RMS for 200 MeV protons in a 2.75 cm (7.4 g cm^{-2}) piece.

If the beam spot was large enough to entirely cover the buckle, then given that the area of the buckle is large (~ 100 cm^2) compared to that of d3mm1 (4.5 cm^2), it seems plausible that the relatively infrequent large-angle scatters are enough to account for the 10-20% of the detected event samples that are attributable to slow protons. That is, a very large number of protons hit the buckle compared to the number hitting d3mm1 directly, and a small percentage of those in the buckle undergo scattering sufficient to deflect them into d3mm1. Their energy is reduced by ionization energy loss in the buckle and an increased pathlength through the first plug.

An essential feature of the experiment is that any hit above threshold in d3mm1 triggered the readout, so that any slow particles that hit d3mm1 but missed the other detectors (because of stopping or scattering) were recorded. On the other hand, slow particles that missed d3mm1 but entered d3mm2 or d3mm3 (presumably at large angles with respect to the nominal beam axis), would not be recorded. This accounts for the significant reduction in the numbers of entries in the d3mm2 and d3mm3 histograms – Fig. 9(b) and 9(c) – compared to the number in d3mm1 in Fig. 9(a).

Because the silicon detector spectra were swamped by low-energy protons, it is difficult to make any estimates of the contributions of recoils or target fragments in this location – the methods devised for the previous runs do not apply well to this data set. However, we note that in Fig. 10, it is clear that the tail of the slow protons in d3mm2 extends up to ΔE of about 23 MeV. If we assume all events with ΔE > 23 MeV in d3mm2 are due to target fragments or recoils, we can get lower bounds on their prevalence and contribution to dose. We find 2.75% of the events with hits above zero in d3mm2

---

[11] The actual distributions are non-Gaussian – there are more high-angle scatters than predicted by this approximation.

satisfy this criterion; fully half of those are in the overflow bin, so we can say only that they had $\Delta E > 33$ MeV. The events below 23 MeV have an average ΔE of 5.10 MeV, the distribution as a whole, 5.81 MeV, so the events above 23 MeV pull the average ΔE up by about 14%. It is necessary to correct this for p-Si interactions in the detector, so we have applied the same method to the bare-beam data at 223 MeV beam energy, and find that the events with $\Delta E > 23$ MeV in that sample pull the average up by 4.5%. Taking this into account, the estimated net increase in dose is 9%. If, as expected, the high-LET particles are mostly produced in the water-equivalent plugs surrounding the detectors – which were the same in all runs – then we would expect to see only small changes in their contribution to dose in going from one location in the phantom to another; hence it is not surprising that the estimated 9% dose increase found here is quite consistent with the 8% net increase estimated for d3mm2 in the phantom's brain (using method (4)).

Even at an energy as low as 55 MeV, a proton's LET is about 1.2 keV/μm, well below the 5 keV/μm threshold of CR-39. If the slow protons were present in the combined TLD/CR-39 exposure, their contributions to dose were integrated in the TLD dose but did not contribute to the estimate of dose ascribed to target fragments (3.4% of the total). The dramatic increases seen in the average ΔE/peak ΔE in our detectors reflect an increase in dose (by factors of about 2) compared to the dose that would be expected were there no source of scattered low-energy protons. In the normalization of the high-LET spectrum in CR-39, the LET of incident beam-energy protons is used to calculate the number of incident protons for a given dose; if present, the slow protons would increase the average LET of the incident particles and consequently affect the normalization.

E. Slice 8: 136 MeV Beam

Figures 9(d)-(f) show the histograms obtained with the 136 MeV beam in the same upper abdominal location. The spectra are qualitatively similar to those in Fig. 9(a)-(c), in that they contain many particles with large ΔE. The fractions of events found in the high-ΔE tails are shown in Table 6, and the average ΔE's in Table 7. The increase in average ΔE/peak ΔE are large, but not quite as large as in the run with the 223 MeV beam. Probably much of this is due to saturation of the electronics; as can be seen in the Fig. 9 histograms, considerably more events in the 136 MeV run appear in the overflow bins than in the 223 MeV run. This is simply because the entire spectrum of particles – including those passing through the LCVG buckle or other scattering source – is shifted to higher ΔE when the beam energy decreases. So, while the saturation of the electronics artificially reduces the values of average ΔE in all data sets, it is a particularly significant effect in this one.

Overall, the lower-energy data are quite consistent with the higher-energy data in the same location. Again, the large flux of low-energy protons scattering into the detectors makes our usual methods of determining the contributions of high-LET particles unusable. We have repeated the analysis described in the preceding section, using d3mm2 and looking at events with $\Delta E > 23$ MeV since this is the largest possible energy deposition from a slow proton that also went through d3mm1. (We note that scatter plots for this data set analogous to those shown in Fig. 10 show the same upward-turning band of events due to slow protons.) We find that the events above 23 MeV in d3mm2 pull the average ΔE of the whole distribution up by 14.3%, compared to 4.0% in the bare-beam run at the same extracted beam energy. This leads to an estimated net dose increase of 10%.

F. Slice 9: 223 MeV Beam

Careful examination of the data obtained in this location shows that the detectors recorded only events with ΔE corresponding to two protons, or higher, in d3mm1; the problem was an erroneously high setting for the trigger threshold in d3mm1. In a scatter plot of ΔE in d3mm3 vs. ΔE in d3mm2, one can select the events with one proton in each detector; these turn out to represent about 7% of the sample. When we examine the d3mm1 spectrum on those events, we find only events with ΔE corresponding to two protons (or higher ΔE). No events were recorded where only a single proton was incident on d3mm1; therefore these data cannot be salvaged, except to determine the locations of the single-proton peaks in d3mm2 and d3mm3. These are found to be 2.22 MeV and 2.58 MeV for d3mm2 and d3mm3 respectively. The result for d3mm2 is anomalously low in view of the 2.40 MeV expected in d3mm2 in the bare-beam run with the same extracted beam energy; any materials on the beamline – as were surely present in this run – will cause the peak ΔE to increase, not decrease. Calculations show that the d3mm3 result is most consistent with a beam energy of 223 ± 10 MeV incident on d3mm1. However, 223 MeV is the nominal energy of the beam at the nozzle, assuming the upstream scattering foils were in place. If there were no additional materials in between the nozzle and the first plug, the energy at d3mm1 would be about 212 MeV, just slightly below the lower limit of the estimated uncertainty. Given that there was at

least some thin material present (the suit fabric and the LCVG fabric), the energy at d3mm1 must in reality be lower than 212 MeV. Thus the d3mm3 peak ΔE is also anomalously low, though not as obviously so as for the d3mm2 peak.

There is another (unlikely) possibility: If the scattering foils were absent, the nozzle energy would be about 247 MeV, and a beam energy of 223 MeV (or even 233 MeV, at the high end of the uncertainty) would be possible even with a significant depth of material in between the nozzle and the first plug.

G. Slice 9: 136 MeV Beam

Good data were obtained in this location with the lower beam energy. The histograms in the top row of Fig. 12 show the spectra in d3mm1-3 with no cuts against pile-up. Significant pile-up peaks are seen, particularly in d3mm2 and d3mm3. The remaining histograms in Fig. 12 are: (second row) d3mm1-3 after pile-up rejection method (1) is applied; (third row, from left to right) d3mm1 after method (3) is applied, then d3mm2 and d3mm3 histograms after method (2) is applied. It is clear that the cuts remove most of the pile-up events. The results using the four methods to obtain the fractions of events found in the high-ΔE tails are shown in Table 8, and the results for average and peak ΔE's are shown in Table 9. The fractions and the values of δΔE appear to represent an intermediate case between the results obtained in the brain and those obtained in slice 8 of the phantom. Because there was significant event pile-up in this run, the average ΔE and δΔE values obtained using method (4) will be pulled up significantly. However, the estimates for fractions of events in the tails using methods (4) and (4') should still be valid, provided (as seems likely) that events with 4 or more protons in coincidence were rare.

The single-proton peak locations are most consistent with calculations where the proton energy at d3mm1 was 120 ± 5 MeV. Assuming the presence of the upstream scattering foils, the nozzle energy of 136 MeV would be reduced to 120 MeV by the 2.7 g cm^{-2} of the first plug. This is marginally consistent with the result obtained with the 250 MeV extracted energy, in that both imply a negligible amount of material in between the nozzle and d3mm1. It is possible that this region of the phantom was shielded only by thin layers of fabric (recall that thinnest parts of the suit consist of about 0.2 g cm^{-2} of material)[12].

With pile-up removal methods (3) and (4), which are the most restrictive, the fractions in the tails are all estimated to be between 3.0% and 3.9%; with methods (2) and (4'), the estimated fractions are in the range 3.8% to 6.6%; and with method (1), the fractions are estimated to be about 10% in d3mm1, 8% in d3mm2, and 10% in d3mm3. The fractions found in d3mm1 are generally larger than in d3mm2 or 3 for a particular method. The fractions with all methods except (1) are all approximately double those found in the phantom's brain; for method (1), the fractions here are about 2.5 times larger than in the brain. Since the beam energy estimate based on the single-proton ΔE peaks shows there was less material in the path of the beam in this location than there was in the brain, there is no reason to expect an increase in the contribution of target fragments/recoils. Rather, given the proximity of slice 9 to slice 8 (center-to-center distance of about 12 cm), these results suggest that the source of the slow protons that reached the detectors when they were in slice 8 also produced slow protons that reached slice 9. This is consistent with the hypothesis that the slow protons were scattered into the detectors from something outside the center of the beam spot: If protons can scatter into the volume of space occupied by the detectors in slice 8, then there must be scattered trajectories that would also reach the detectors when placed in slice 9. That there are apparently fewer slow protons in slice 9 suggests that the scattering source was closer to slice 8.

Additional evidence for the presence of slow protons comes from examining the scatter plot of ΔE in d3mm2 vs. ΔE in d3mm1, shown in Fig. 13. The upward-turning band of events indicated in the figure is similar to that seen in Fig. 10. Given the presence of slow protons, we again opt to estimate the dose increase from high-LET particles using events with ΔE > 23 MeV in d3mm2. The events above 23 MeV pull the average up by 10.7%; dividing by the 4.0% increase seen in the comparable bare-beam data (i.e., accounting for p-Si reactions), we find a net dose increase of 6.4%.

---

[12] The estimate of 120 ± 5 MeV for the proton energy at d3mm1 also allows for the possibility that the scattering foils were not present, as per the discussion in the preceding section; if both foils were absent, the nozzle energy would have been 150 MeV and up to 5 cm of water-equivalent material (including the first plug) could have been present between the nozzle and d3mm1. While this scenario cannot be ruled out, there is also no particular reason to suspect the scattering foils were absent for this run.

We have shown evidence of low-velocity protons hitting the silicon detectors during the runs in slices 8 and 9; the energies were far below the nominal beam energies. If it can be demonstrated that there was no piece of the spacesuit in the beam that is thick enough to account for the observed energy losses, then another explanation is required. It is conceivable that the beam was scraping off one of the apertures in the transport line downstream of the last bending magnet. By scraping we mean that some of the beam particles traversed more material than intended, e.g., a housing of one of the beam-monitoring detectors or the inner wall of the beam pipe itself.

As described above, the comparatively tiny beam currents required for satisfactory performance of the silicon detectors were too small for the operator to monitor the beam directly. Also, just prior to the runs with the detectors in the abdominal area of the phantom, beam was lost due to a power supply fault in the beam switchyard. Recovery from the fault was difficult and time-consuming, and there was not sufficient time remaining[13] to remove the detectors from the phantom and perform a diagnostic bare-beam run. It may be that in recovering the beam without the usual feedback signals available, the operator was unable to steer the beam properly and some portion of it was slowed by scraping. Scraping protons would also tend to scatter much more than those that followed straight trajectories through the beamline; this could account for the highly-divergent beam seen in the abdominal data, particularly the slice-8 data.

I. Summary of Results With Detectors in the Phantom

The results obtained in the preceding sub-sections are summarized in Table 10. Despite the complicated steps needed to extract the information, the results are generally consistent with our physical picture of energy deposition from protons and nuclear interaction products. We estimate that the 155 MeV extracted beam produces dose contributions from target fragments in the 2 to 10% range, and the 250 MeV extracted beam produces contributions in the 8 to 10% range. These results have large systematic uncertainties associated with them, perhaps as large as 50%, but they are at least of the same order of magnitude as the dose increases measured in CR-39, and the 8-9% estimate obtained in the phantom's brain agrees well with the 7.6% found in the CR-39 data with the same beam and detector location.

In addition to the dose increases from high-LET secondaries, doses at depth increase due simply to the higher LET of the primary beam protons as their energy decreases. Using the calculated proton energies incident on d3mm1 in each location in the phantom, we have calculated the proton LET at depth; the ratio of that LET to the bare-beam LET (i.e., the LET of the beam as it exits the nozzle) is shown, for each location, in the bottom row of Table 10. As one would expect, the ratios are all higher for the beam with 136 MeV nozzle energy; the effect is particularly pronounced in the brain location. Because it was at the greatest depth in tissue, this location was ostensibly the most shielded; however, these results clearly show that the materials in front of the detectors cause dose increases, not just from high-LET secondaries, but also by slowing the incident protons so that their LETs (and hence doses per particle) increase significantly. In slice 8, where there was considerably less material in front of the detectors, the dose increase due to the slowing of the protons is smaller than that due to high-LET secondaries for the 223 MeV beam; the opposite is true for the 136 MeV beam in this location. In slice 9, where the shielding was minimal, the two effects are of roughly equal importance with the 136 MeV beam.

It is clear that, with protons as energetic as the ones used in this experiment, the usual relation between increased shielding and reduced dose does not apply. Materials in front of a given point in the body – whether they are the walls of a spacecraft, or a spacesuit, or the body's own tissue – cause the doses from such high-energy particle to increase at points deep in the body. This is a result of both of the mechanisms described above, the production of target fragments/recoils, and the increased LET of protons as they slow significantly at depth in tissue.

5. CONCLUSIONS

Deposited energy spectra have been measured with the LLUMC proton beams incident on unshielded silicon detectors and on the same detectors placed in three locations inside a human phantom that was shielded by the EMU spacesuit. The locations of single-proton peaks have been used to determine the incident energies at the first detector (d3mm1), and these

---

[13] The measurements were performed in between the end of one day's patient treatments and the beginning of the next, severely constraining the time available for these runs.

have in turn been used to estimate the depth of water-equivalent material interposed between the nozzle and d3mm1. The data show that a considerable depth of material, about 9.5 cm of water-equivalent, was present upstream of d3mm1 in the brain location. Of this, 2.7 cm was in a plug of material immediately in front of d3mm1. Presumably, most of the rest is attributable to the phantom's skull. Less material, approximately 4.5 cm water-equivalent depth, was present when the detectors were placed in the upper abdominal position in the phantom (slice 8); again, 2.7 cm of this was in the plug in front of d3mm1. In slice 9, the data are consistent with 2.7 cm water-equivalent depth in front of d3mm1; this implies a negligible amount of material in between the nozzle and the plug in front of d3mm1.

Compared to CR-39 detectors, the silicon detectors are thick and have large volume, making them unsuitable for measuring the LET spectra of low-energy particles that do not traverse the full detector depth, or that are incident at a large angle with respect to the nominal beam axis; unfortunately, this describes many of the target fragments and recoils produced in nuclear interactions of protons with nuclei in the spacesuit and phantom materials. Nonetheless, because the detectors accurately record the energy deposited in them by beam protons and any target fragments or recoils that reach them, it is reasonable to use them to estimate dose. Elaborate procedures have been developed to make these estimates, accounting for the contributions expected from protons interacting in the detectors and for other complicating features in the data such as event pile-up and the slow protons seen in slice 9 and especially slice 8. The results are estimates with considerable uncertainties, but they show internal consistency and are in reasonable accord with the CR-39 measurements.

The fact that protons at these energies can produce a flux of high-LET secondary particles has important implications for possible future improvements to the shielding properties of spacesuits to be worn on EVA's. Adding mass to the suits would stop more of the low-energy electron and proton flux, which would have the desirable effect of reducing the dose to the skin and other shallow points in the body. However, this would also have the consequence of increasing the build-up of secondaries and thus increasing the dose at greater depth. The optimal design (i.e., the one that leads to the greatest overall reduction in risk) will have to balance these competing factors, while taking into account the detailed composition of the incident radiation field and the variations in radiation sensitivity of different organs.

APPENDIX – NUCLEAR INTERACTIONS IN SILICON

We first consider p-Si reactions in the rest frame of the proton. Preliminary data obtained by our group [23] with a 600 MeV/nucleon ^{28}Si beam yield a cross section of 374 ± 11 mb, in excellent agreement with the value of 379 ± 6 mb reported by Webber *et al.* [24] at 500 MeV/nucleon. The semi-empirical nuclear cross section model NUCFRG2 [25] predicts a charge-changing cross section of 368 mb at 250 MeV/nucleon. In the rest frame of the silicon (the laboratory frame for the present experiment), a cross section of 374 mb yields a mean free path of 53 cm for protons in silicon. In a 3 mm thick detector, therefore, 0.57% of incident protons are expected to undergo an interaction in which a silicon nucleus is broken up.

Elastic reactions are also expected to contribute to the high-ΔE tails in the detected spectra; in these reactions, the projectile scatters and the target nucleus recoils, leaving a short track in the detector. For instance, a recoiling silicon nucleus with 1 MeV/nucleon kinetic energy has a range of about 3 μm and will deposit all 28 MeV of its total energy in

the detector. At 250 MeV, the proton-proton cross section is entirely due to elastic scattering, and has a value of about 20 mb, very near its minimum. Using the empirical scaling law defined in Ref [17], the elastic scattering cross section for protons on silicon is predicted to be $\sigma_{p-Si} = \sigma_{p-p} A_{Si}^{0.77} = 260$ mb (with $A_{Si} = 28$). Added to the fragmentation cross section of 374 mb, the total cross section $\sigma_{tot} = \sigma_{inel} + \sigma_{el} = 634$ mb. A recent calculation of σ_{tot} for protons on aluminum [25] predicts a value of 580 mb, in agreement with experimental data; assuming a power-law scaling in A_{targ}, this predicts σ_{tot} for protons on silicon of about 600 mb, within 6% of our estimate.

Using 260 mb for the elastic cross section gives a mean free path for elastic reactions of 76.8 cm, so that 0.39% of incident protons will undergo an elastic reaction with a silicon nucleus in a 3 mm depth. Combined with the 0.57% of protons predicted to cause fragmentation of a silicon nucleus, we expect a total of 0.96% of protons to interact in a detector. The Si fragmentation cross section is expected to be weakly dependent on beam energy, and the proton-proton elastic cross section increases only slightly in going from 250 MeV to 155 MeV; therefore only a small change in the fraction of high-ΔE events is expected at the lower beam energy.

REFERENCES

1. NCRP Report No. 98, *Guidance on Radiation Received in Space Activities*, National Council on Radiation Protection and Measurements (1989). See especially pp. 15-24.
2. M. F. Moyers, in "Proton Therapy" in The Modern Technology of Radiation Oncology: A Compendium for Medical Physicists and Radiation Oncologists, ed. J. vanDyk, Wisconsin: Medical Physics Publishing, (1999) p. 823 - 869.
3. M. F. Moyers, G. A. Nelson, and P. Saganti, *Med. Phys*. **27** (6), 1405 (2000).
4. J. W. Wilson, J. Tweed, C. Zeitlin, M.-H. Y. Kim, B. Anderson, F. A. Cucinotta, J. Ware, and A. E. Persans, SAE Paper Number 01ICES-299.
5. J. D. Bowman, W. J. Swiatecki, and C. F. Tsang, Lawrence Berkeley Laboratory No. LBL-2908, 1973.
6. ICRP Publication 60, *1990 Recommendation of the International Commission on Radiological Protection*, Pergammon Pres (1991).
7. E. Benton, Eril Research, Inc., Report No. ERI-000501.
8. T. Doke *et al*., *Radiat. Meas*. **24**, (1) 75 (1995).
9. E. Benton, private communication.
10. C. Zeitlin, K.A. Frankel, W. Gong, L. Heilbronn, E.J. Lampo, R. Leres, J. Miller, W. Schimmerling, *Radiat. Meas*., **23**, No. 1, 65-81 (1994).
11. C. Zeitlin, L. Heilbronn, J. Miller, L. Heilbronn, K. Frankel, W. Gong and W. Schimmerling, *Radiat. Res*. **145**, 655-665 (1996).
12. C. Zeitlin, L. Heilbronn, J. Miller, S. E. Rademacher, T. Borak, T.R. Carter, K. Frankel, W. Schimmerling and C. E. Stronach, *Phys. Rev. C***56,** 388-397 (1997).
13. C. Zeitlin, L. Heilbronn, and J. Miller, *Radiat. Res*. **149**, 560-569 (1998).
14. C. Zeitlin, A. Fukumura, L. Heilbronn, Y. Iwata, J. Miller, and T. Murakami, Lawrence Berkeley National Laboratory Report No. 45771 (2000), and *Phys. Rev*. C (in press).
15. S.W. Alderson, L.H. Lanzl, M. Rollins, and J. Spira. *The American Journal of Roentgenology, Radium Therapy, and Nuclear Medicine*, Vol. 87(1), 185 (1962).
16. A detailed description and specifications of the Amptek A225 chip can be found on the World Wide Web at http://www.amptek.com/a225.html
17. Particle Data Group, D. E. Groom *et al*., *European Physical Journal* C **15,** 1 (2000). See Sec. 23.2 for a detailed discussion.
18. M. F. Moyers, private communication.
19. S. M. Selzer and M. J. Berger, Technical Report SP 3012, NASA, 1964.
20. W. B. Christie et al., *Nucl. Instr. Meth.*, A**225** 466-476 (1987).

21. The ESTAR program was used. ESTAR was written by M. J. Berger of the National Institute of Standards and Technology, and can be found (and run interactively) on the World Wide Web at: http://physics.nist.gov/PhysRefData/Star/Text/ESTAR.html.
22. C. Zeitlin, A. Fukumura, L. Heilbronn, Y. Iwata, J. Miller, and T. Murakami, Lawrence Berkeley National Laboratory Report No. 47655 (2001).
23. W. R. Webber, J. C. Kish and D. A. Schrier, *Phys. Rev.* C **41**, 533 (1990).
24. J. W. Wilson, J. L. Shinn, L. W. Townsend, R. K. Tripathi, F. F. Badavi, and S. Y. Chun, *Nucl. Instr. Meth.* B **94**, 95 (1994).
25. R. K. Tripathi, J. W. Wilson, and F. A. Cucinotta, NASA TP-2000-210534.

Method	% of events in high-ΔE tail 223 MeV beam			% of events in high-ΔE tail 145 MeV beam		
	d3mm1	d3mm2	d3mm3	d3mm1	d3mm2	d3mm3
1	0.5	0.7	1.1	0.5	0.8	1.1
2	—	0.7	1.1	—	0.8	1.1
3	0.3	—	0.9	0.2	—	0.8
4	0.7	0.8	0.8	0.6	0.8	0.8

Table 1. Fractions of events found in the high-ΔE tails of the distributions in the three detectors for the two highest-energy beams. The fractions depend on the pile-up rejection method and the corresponding definition of the tail. A detailed explanation is in the text. The statistical errors associated with these results are in all cases in the range from 2% to 6% of the values shown in the table.

Det. #	ΔE peak (MeV)	Calc 223 MeV	ΔE peak (MeV)	Calc 145 MeV	ΔE peak (MeV)	Calc 60 MeV	ΔE peak (MeV)	Calc 41 MeV
1	2.27	2.40	3.19	3.19	6.34	6.33	9.1	9.0
2	2.18	2.40	3.15	3.23	6.84	6.96	11.5	11.8
3	2.25	2.43	3.30	3.30	8.10	7.96	16.5	19.4

Table 2. Deposited energy in MeV for d3mm1, 2, and 3 with the bare beam (left-most columns), compared to calculations with beam energies as shown assuming dead layers were 2% of detector thickness. Quoted beam energies are the nozzle energies, determined by iterating the calculation until agreement with data was obtained. The result for d3mm3 with the 41 MeV is an exceptional case, as explained in the text. The ratios between calculated and measured ΔE's in the 223 MeV run were used as correction factors for the data values in the other runs.

	PUR method	223 MeV beam			145 MeV beam		
		ΔE Avg. (MeV)	δΔE (%)	RMS (MeV)	ΔE Avg. (MeV)	δΔE (%)	RMS (MeV)
d3mm1	1	2.54	6	1.55	3.32	4	1.41
	3	2.49	2	1.08	3.25	2	0.86
	4	2.73	14	1.97	3.58	12	1.94
	p peak	2.40	—	0.26	3.19	—	0.33
d3mm2	1	2.58	8	1.76	3.32	5	1.79
	2	2.59	9	1.77	3.30	5	1.78
	4	2.68	13	1.42	3.57	13	2.19
	p peak	2.38	—	0.29	3.15	—	0.43
d3mm3	1	2.66	9	1.85	3.54	7	1.84
	2	2.66	9	1.84	3.51	6	1.80
	3	2.62	7	1.71	3.48	5	1.69
	4	2.81	15	2.03	3.76	14	2.11
	p peak	2.44	—	0.28	3.30	—	0.34

Table 3. Average ΔE values for the three detectors and four methods of pile-up rejection, for the 223 and 145 MeV (nozzle energies) bare-beam runs. Also shown are the percent increases in the averages compared to the proton peak ΔE's (δΔE) and RMS's of the distributions.

	223 MeV beam % of events in high-ΔE tail			136 MeV beam % of events in high-ΔE tail		
Method	d3mm1	d3mm2	d3mm3	d3mm1	d3mm2	d3mm3
1	4.6	3.0	3.7	3.2	0.6	—
2	—	2.6	3.2	—	0.5	—
3	1.3	—	2.3	0.4	—	—
4 ($4\Delta E_p$)	2.0	1.7	1.4	0.8	< 1.4	—
4' ($3\Delta E_p$)	2.6	2.6	2.3	1.7	< 1.4	—

Table 4. Fractions of events found in the high-ΔE tails of the distributions in the three detectors for the runs using the EMU helmet and the phantom's head. The 136 MeV beam stopped in the water-equivalent plastic between d3mm2 and d3mm3, hence there are no data for d3mm3.

	223 MeV						136 MeV					
	d3mm1		d3mm2		d3mm3		d3mm1		d3mm2		d3mm3	
PUR Method	Avg. ΔE (MeV)	δΔE (%)	Avg. ΔE (MeV)	δΔE (%)	Avg. ΔE (MeV)	δΔE (%)	Avg. ΔE (MeV)	δΔE (%)	Avg. ΔE (MeV)	δΔE (%)	Avg. ΔE (MeV)	δΔE (%)
1	3.22	20	3.22	11	3.62	18	6.26	9	13.9	10	—	—
2	—	—	3.19	10	3.55	15	—	—	14.6	15	—	—
3	2.84	6	—	—	3.51	14	6.04	5	—	—	—	—
4	3.35	24	3.54	22	3.85	25	6.57	14	14.6	15	—	—
p peak	2.69	—	2.89	—	3.08	—	5.75	—	12.7	—	—	—

Table 5. Average ΔE's in the three detectors using the four methods of pile-up rejection (PUR) for the runs using the EMU helmet and the phantom's head. The influence of the high-ΔE tails on the distributions is estimated by δΔE, the percentage increase in the average ΔE over the ΔE of the single-proton peak (shown in the bottom row) in the same spectrum.

Method	223 MeV beam % of events in high-ΔE tail			136 MeV beam % of events in high-ΔE tail		
	d3mm1	d3mm2	d3mm3	d3mm1	d3mm2	d3mm3
2	—	17.5	27.1	—	21.6	31.9
3	9.7	—	20.1	8.0	—	21.6
4 ($4\Delta E_p$)	10.6	11.9	12.6	5.8	7.6	12.2
4' ($3\Delta E_p$)	16.1	18.5	20.3	10.4	13.6	18.1

Table 6. Fractions of events found in the high-ΔE tails of the distributions in the three detectors for the runs in slice 8 of the phantom, the upper abdomen. Pile-up rejection method (1) was not applicable to these data.

PUR Method	223 MeV						136 MeV					
	d3mm1 Avg. ΔE (MeV)	$\delta\Delta$E (%)	d3mm2 Avg. ΔE (MeV)	$\delta\Delta$E (%)	d3mm3 Avg. ΔE (MeV)	$\delta\Delta$E (%)	d3mm1 Avg. ΔE (MeV)	$\delta\Delta$E (%)	d3mm2 Avg. ΔE (MeV)	$\delta\Delta$E (%)	d3mm3 Avg. ΔE (MeV)	$\delta\Delta$E (%)
2	—	—	4.47	70	5.26	94	—	—	6.76	70	10.5	74
3	3.65	36	—	—	4.67	73	4.56	25	—	—	9.02	50
4	5.39	108	5.81	121	6.14	127	5.84	60	7.34	84	11.6	92
p peak	2.59	—	2.63	—	2.70	—	3.64	—	3.98	—	6.03	—

Table 7. Average ΔE's in the three detectors using three of the four methods of pile-up rejection (PUR) for the runs in phantom slice 8.

23

	136 MeV beam % of events in high-ΔE tail		
Method	**d3mm1**	**d3mm2**	**d3mm3**
1	9.9	7.7	10.0
2	—	3.8	6.6
3	3.4	—	3.0
4 (4ΔEₚ)	3.9	3.1	3.0
4' (3ΔEₚ)	5.9	5.6	5.4

Table 8. Fractions of events found in the high-ΔE tails of the distributions in the three detectors for the runs in slice 9 of the phantom, the lower abdomen.

	136 MeV					
	d3mm1		**d3mm2**		**d3mm3**	
	Avg.		**Avg.**		**Avg.**	
PUR	**ΔE**	**δΔE**	**ΔE**	**δΔE**	**ΔE**	**δΔE**
Method	**(MeV)**	**(%)**	**(MeV)**	**(%)**	**(MeV)**	**(%)**
1	5.77	45	5.11	29	6.54	35
2	—	—	4.61	16	5.95	22
3	4.71	18	—	—	5.48	13
4	6.11	54	6.19	56	7.31	50
p peak	3.98	—	3.96	—	4.86	—

Table 9. Average ΔE's in the three detectors using the four methods of pile-up rejection (PUR) for the runs in phantom slice 9.

	Brain	Slice 8	Slice 9
E_{nozzle} = 223 MeV	$E_{d3mm1} = 181 \pm 5$	$E_{d3mm1} = 205 \pm 5$	$E_{d3mm1} = 223 \pm 10$
E_{nozzle} = 136 MeV	$E_{d3mm1} = 66 \pm 2$	$E_{d3mm1} = 105 \pm 5$	$E_{d3mm1} = 123 \pm 5$
Estimated water-equiv. material before d3mm1	9.5 cm	4.5 cm	2.7 cm
Estimated dose contribution from high-LET particles	**223:** 8-9% **136:** 2-5%	**223:** 9% **136:** 10%	— **136:** 6%
Proton Peak LET ratio, *in situ*/nozzle	**223:** 1.14 ± 0.02 **136:** 1.71 ± 0.04	**223:** 1.05 ± 0.02 **136:** 1.21 ± 0.04	**223:** 1.00 ± 0.03 **136:** 1.07 ± 0.03

Table 10. Top two rows: Calculated values of incident energy at d3mm1 for the two beam energies and three locations in the phantom. (All energies are in MeV.) Third row: Water-equivalent depth estimates based on the proton peak ΔE's; depths include the 2.7 cm of water-equivalent plastic comprising the plug in front of d3mm1. Fourth row: Estimated increase in dose due to high-LET target fragments and recoils. Bottom row: Ratios of LET's of the protons at depth to LET's at the nozzle for the 223 MeV and 136 MeV nozzle energies. The estimated dose contributions from high-LET particles are in addition to the dose increases from ionization energy loss increases along the Bragg curve.
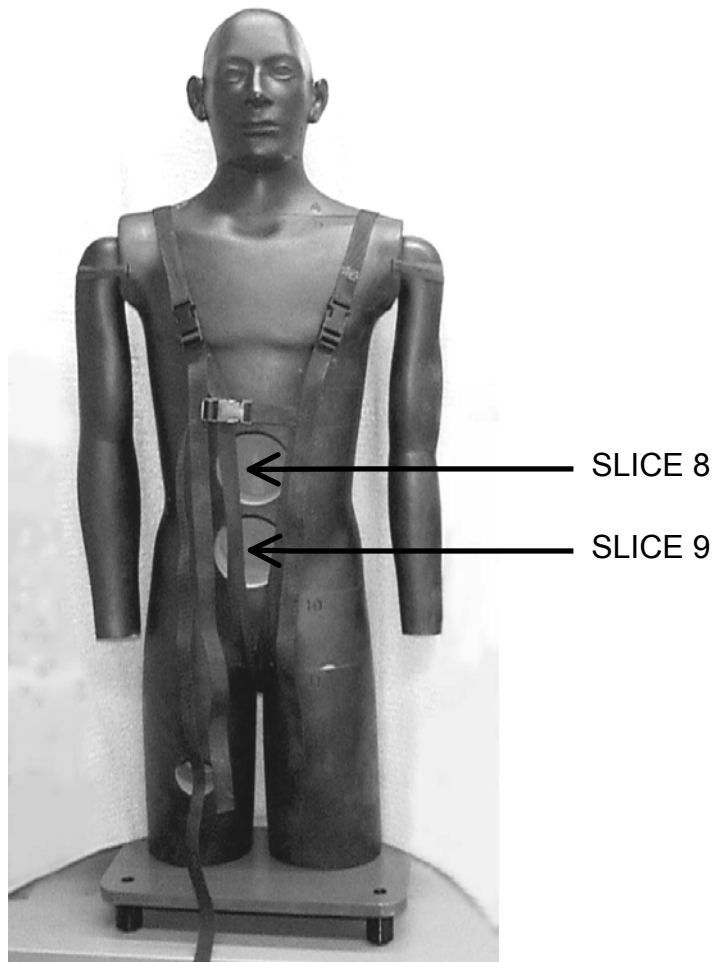
Figure 1. The human phantom used in conjunction with the EMU spacesuit. Two of the pre-drilled holes to accommodate detectors are shown. The phantom is modular and can be separated into "slices."
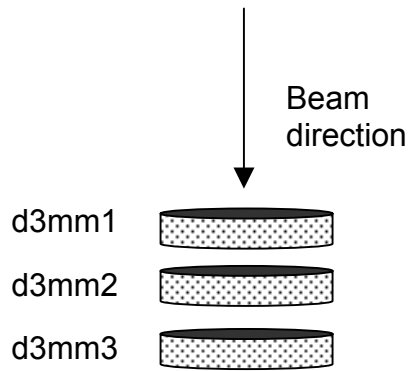
Figure 2(a). Sketch of the detector configuration for the bare-beam runs. The air gaps between detectors were approximately 1 cm.
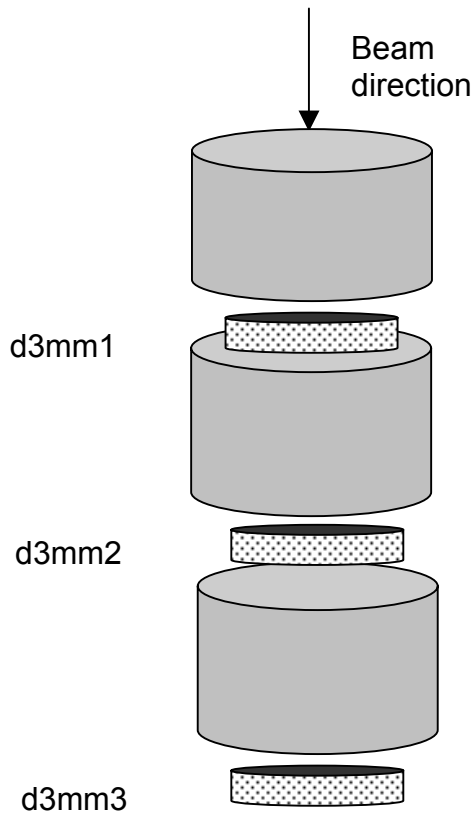

Figure 2(b). Sketch of the detector configuration for the runs with the detectors placed in the phantom, enclosed by the corresponding piece of the EMU spacesuit. The plug in front of d3mm1 was 27 mm deep, the others 22 mm. The pieces shown were encased in a larger cylinder (not shown) of water-equivalent plastic (hollow along its central axis to hold the detectors and plugs), and placed in the phantom.

27
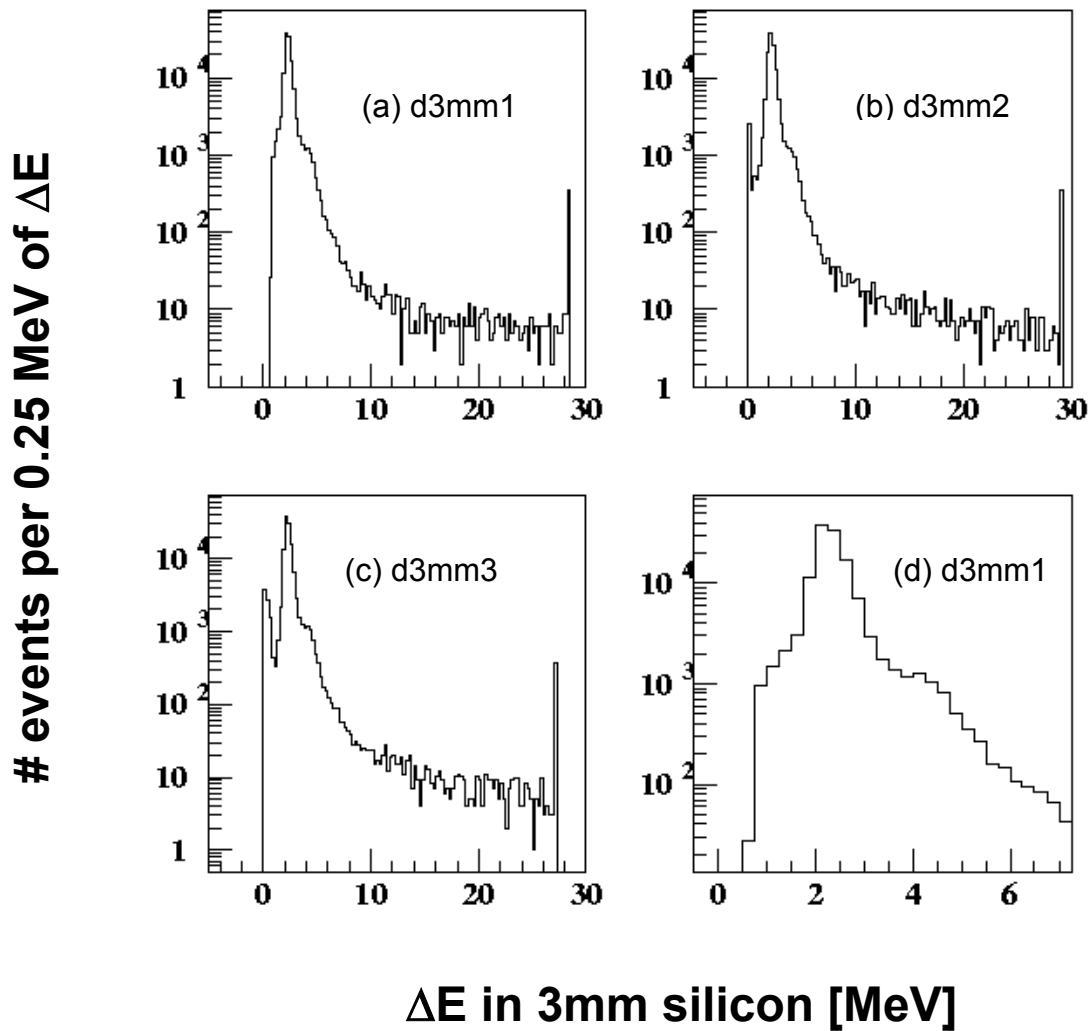
Figure 3. Histograms of ΔE in the three detectors for the bare-beam run with an extracted beam energy of 250 MeV. In (d) we focus on the proton peak region of d3mm1, in order to clearly show the pile-up peak near 4 MeV.
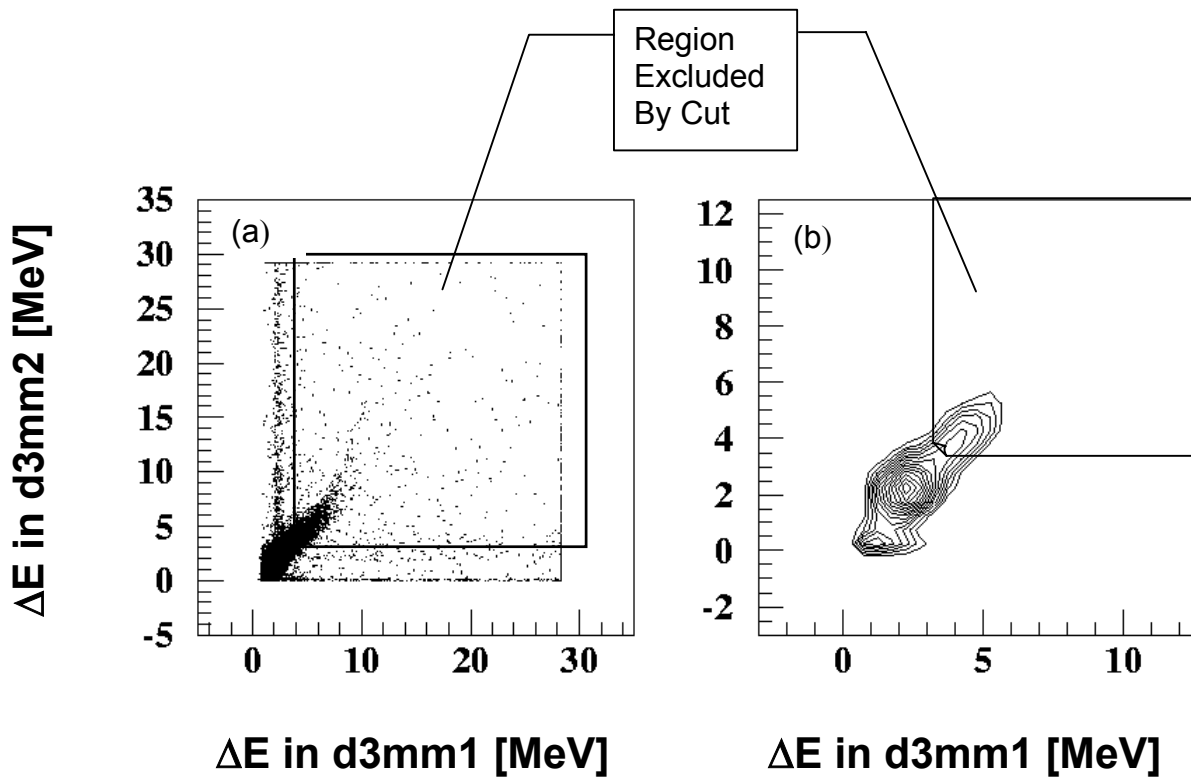
Figure 4. Scatter plots of d3mm2 vs. d3mm1 for the same event sample as in Fig. 3, where the only requirement is a hit well above threshold in d3mm1. Fig. 4(a) shows a concentration of events along the 45° line, indicating both detectors were hit by the same particle or particles. The rectangle superimposed on the data indicates the region excluded by a graphical cut. Fig. 4(b) shows the same events in the region below 12 MeV in each detector, plotted as contours on a logarithmic-sensitivity scale. Denser contours represent higher concentrations of events.

After pile-up removal method (1).
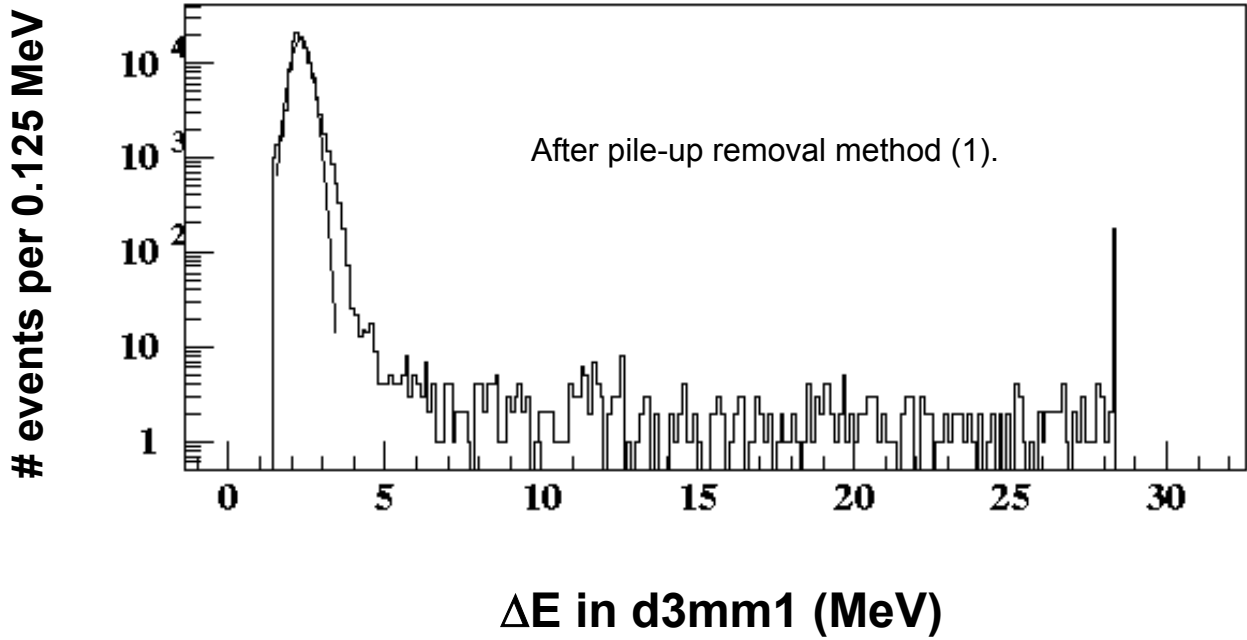
Figure 5. Histogram of ΔE in d3mm1 after application of a pile-up rejection cut based on the scatter plot method described in the text. The curve shown is the best-fitting Gaussian in the central bins of the main proton peak. Data are from the run with a beam energy of 250 MeV at extraction.
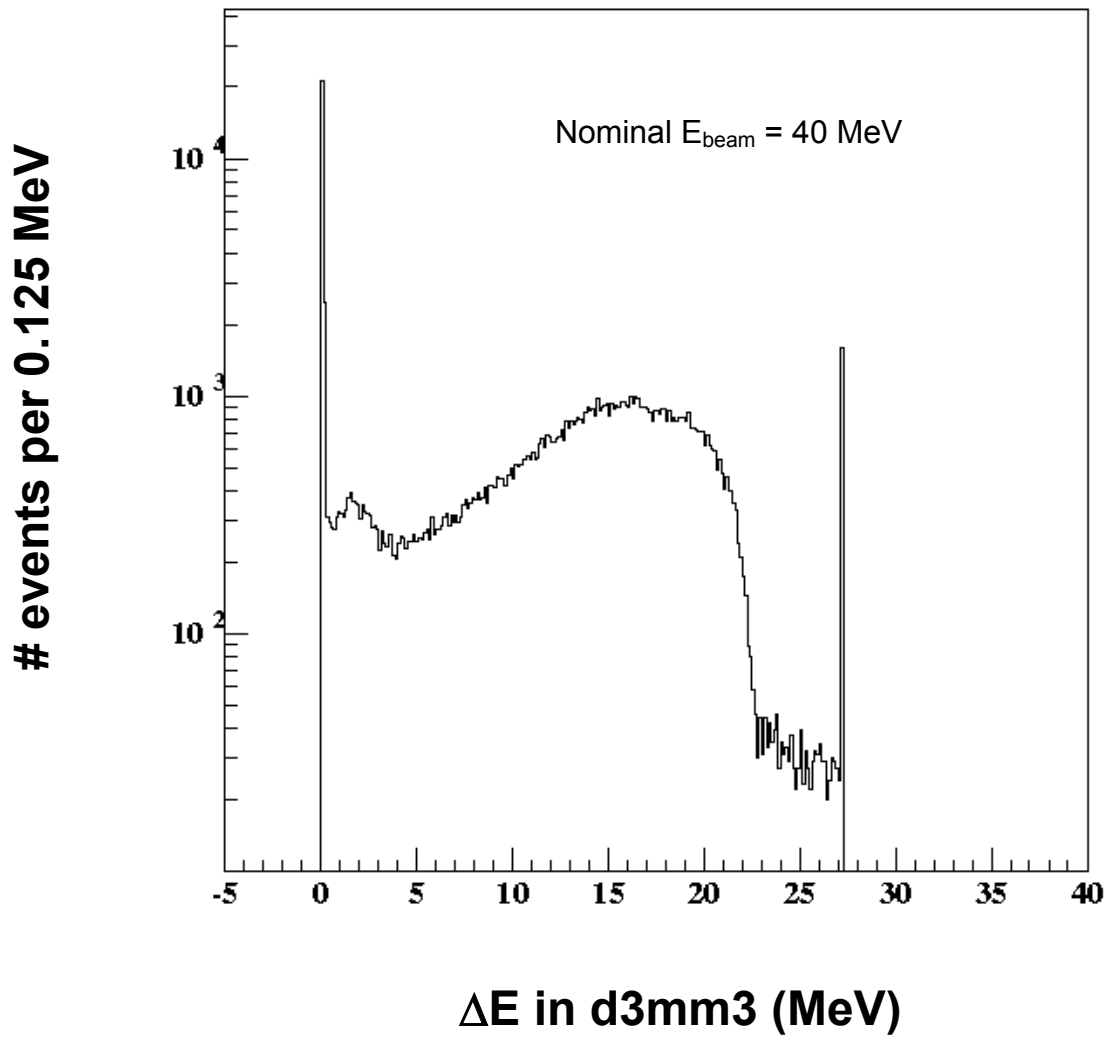
Figure 6. Deposited energy in d3mm3 in the 40 MeV run. Comparison of measured and calculated ΔE's indicates the actual energy may have been 41 MeV. The broad distribution seen here is due to straggling.
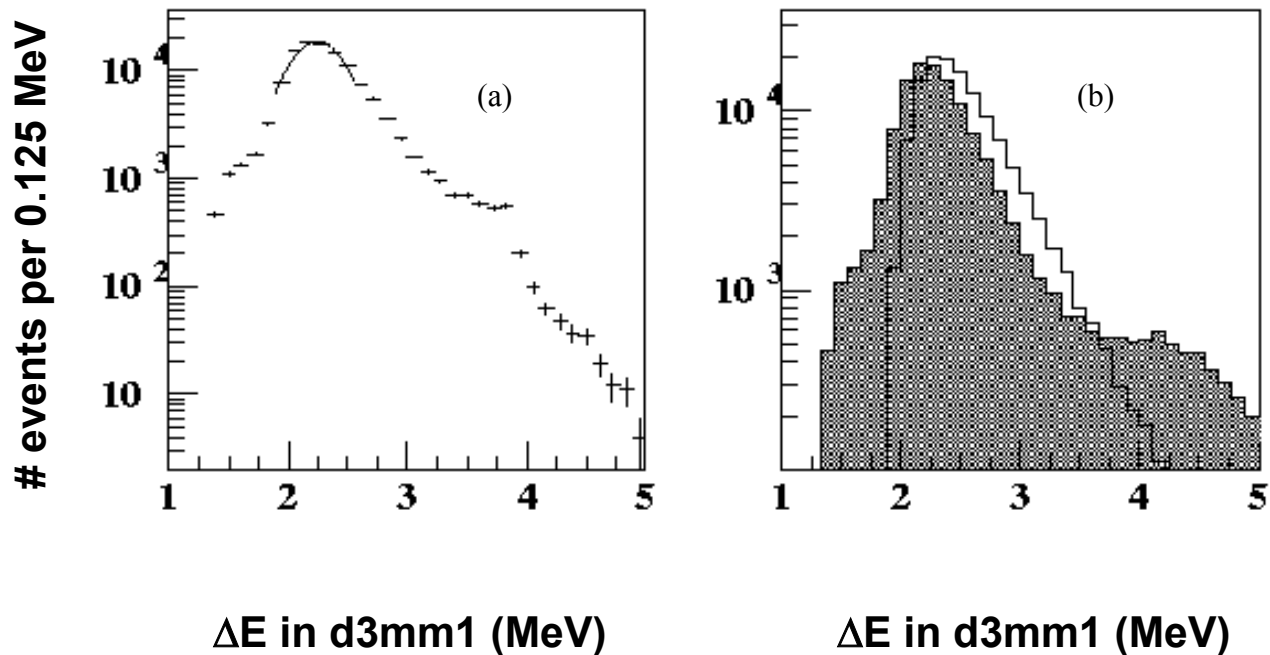
Figure 7. Histograms of the peak region in d3mm1. In 7(a), a Gaussian distribution fit to the center of the peak is shown as a curve, and the data are shown as points with error bars (in the center of the peak, the error bars are too small to be visible on this scale). In 7(b), the data are shown as a shaded histogram, and a histogram corresponding to a Landau distribution is superimposed.
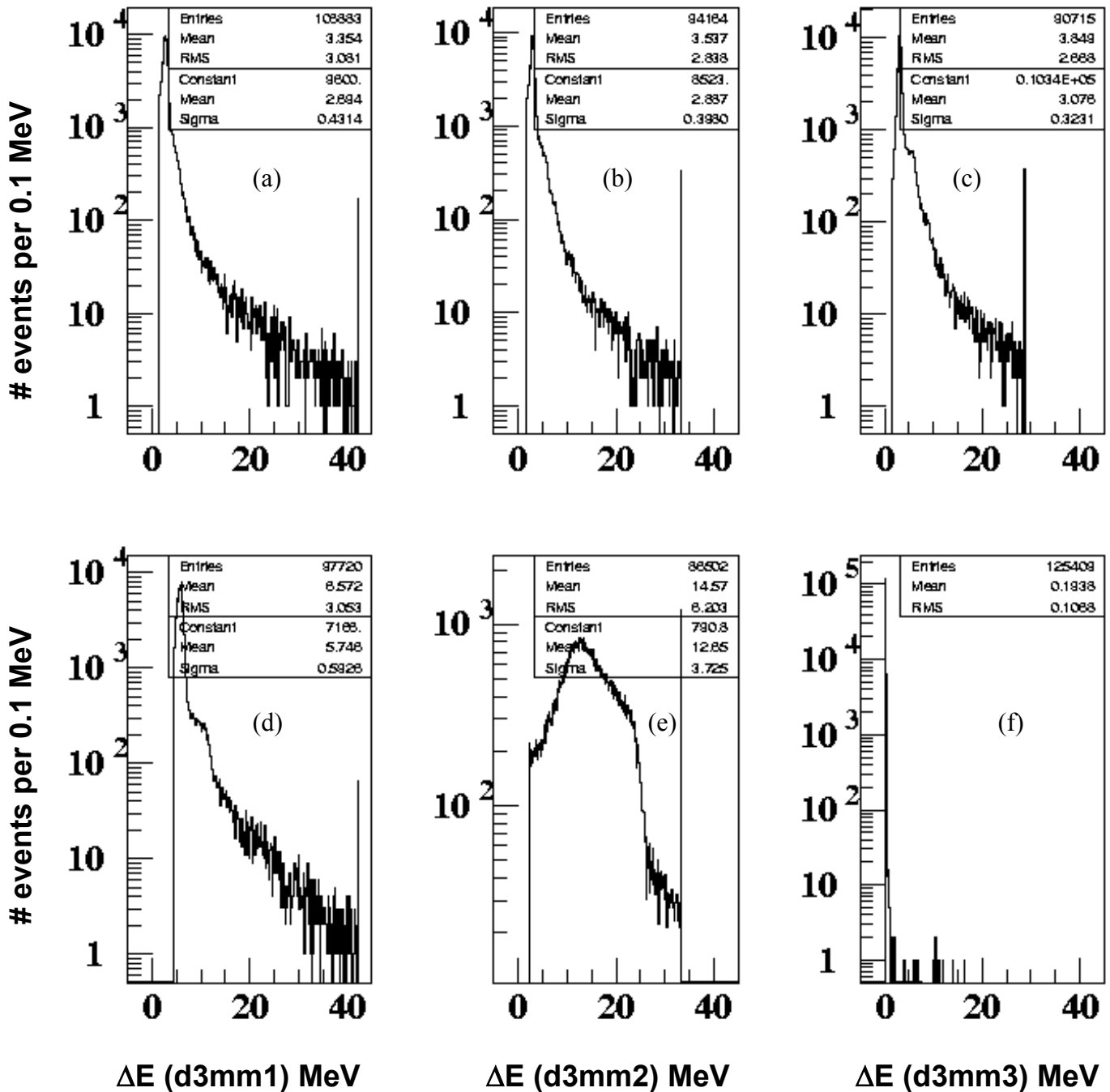
events per 0.1 MeV

(a)

Entries	108883
Mean	3.354
RMS	3.081
Constant1	9600.
Mean	2.894
Sigma	0.4314

(b)

Entries	94164
Mean	3.537
RMS	2.838
Constant1	8523.
Mean	2.887
Sigma	0.3980

(c)

Entries	90715
Mean	3.849
RMS	2.668
Constant1	0.1034E+05
Mean	3.076
Sigma	0.3231

(d)

Entries	97720
Mean	6.572
RMS	3.053
Constant1	7166.
Mean	5.746
Sigma	0.5926

(e)

Entries	86502
Mean	14.57
RMS	6.203
Constant1	790.3
Mean	12.65
Sigma	3.725

(f)

Entries	125409
Mean	0.1936
RMS	0.1066

ΔE (d3mm1) MeV ΔE (d3mm2) MeV ΔE (d3mm3) MeV

Figure 8. The top row, 8(a)-(c), shows histograms of ΔE in (from left to right) d3mm1, 2, and 3 for the 250 MeV extracted beam incident on the EMU helmet with detectors placed in the position corresponding to the brain. In each histogram, ΔE in that detector was required to be above 1.4 MeV to guarantee that the detector was hit by a beam proton and/or a secondary. Text boxes show the numbers of entries, means and RMS's of the entire distribution, and the parameters (constant, mean, and standard deviation) found by Gaussian fits to the central bins of the proton peaks. Bottom row, 8(d)-(f): Corresponding histograms with the 155 MeV extracted beam.
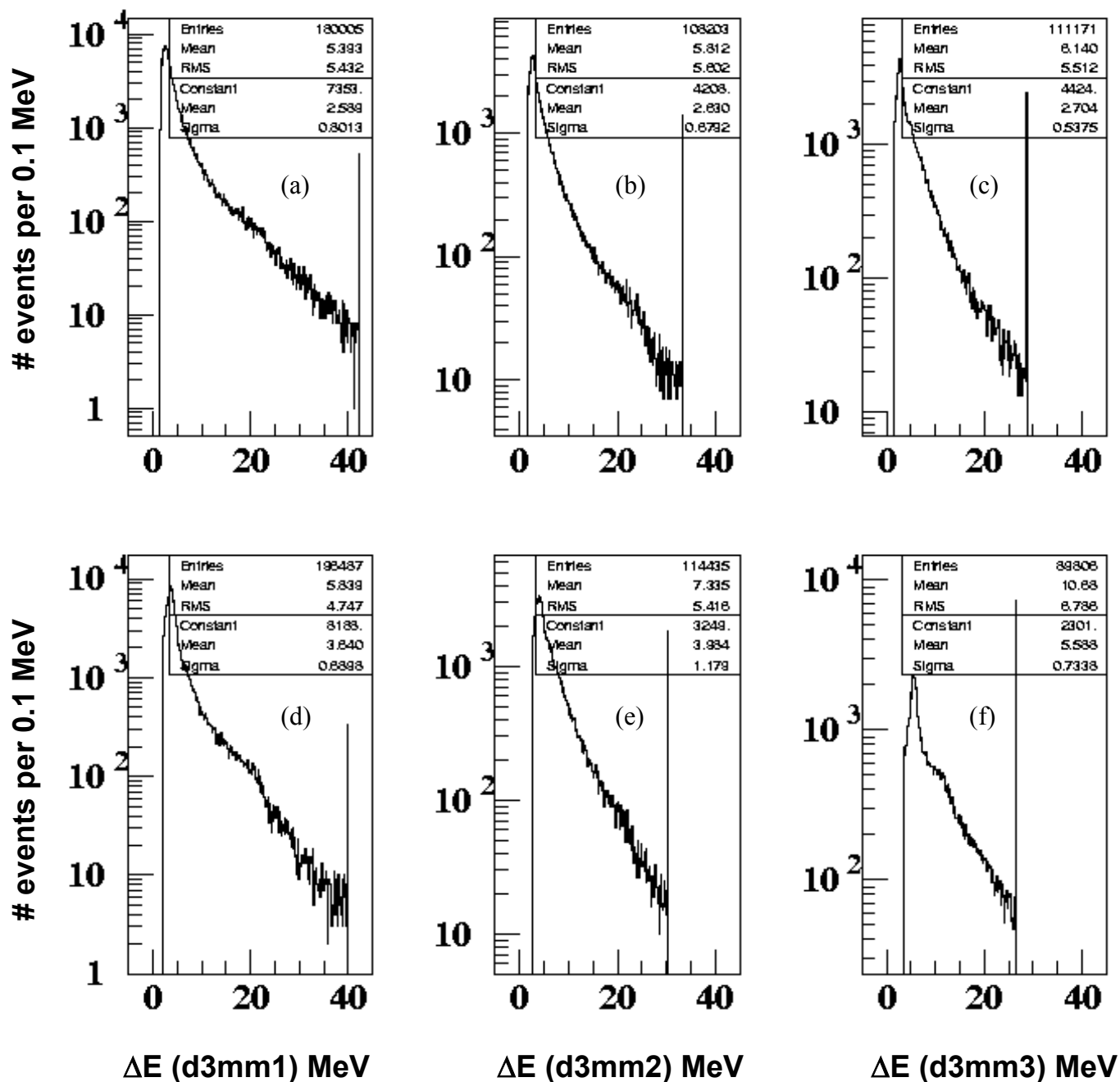
Figure 9. Top row: Histograms of ΔE in d3mm1, 2, and 3 for the 250 MeV extracted beam incident with detectors placed in the phantom's upper abdomen (slice 8). Bottom row: Corresponding histograms for the run with the 155 MeV extracted beam. In each case, ΔE averaged over the entire distribution is far larger than that of the single-proton peak.
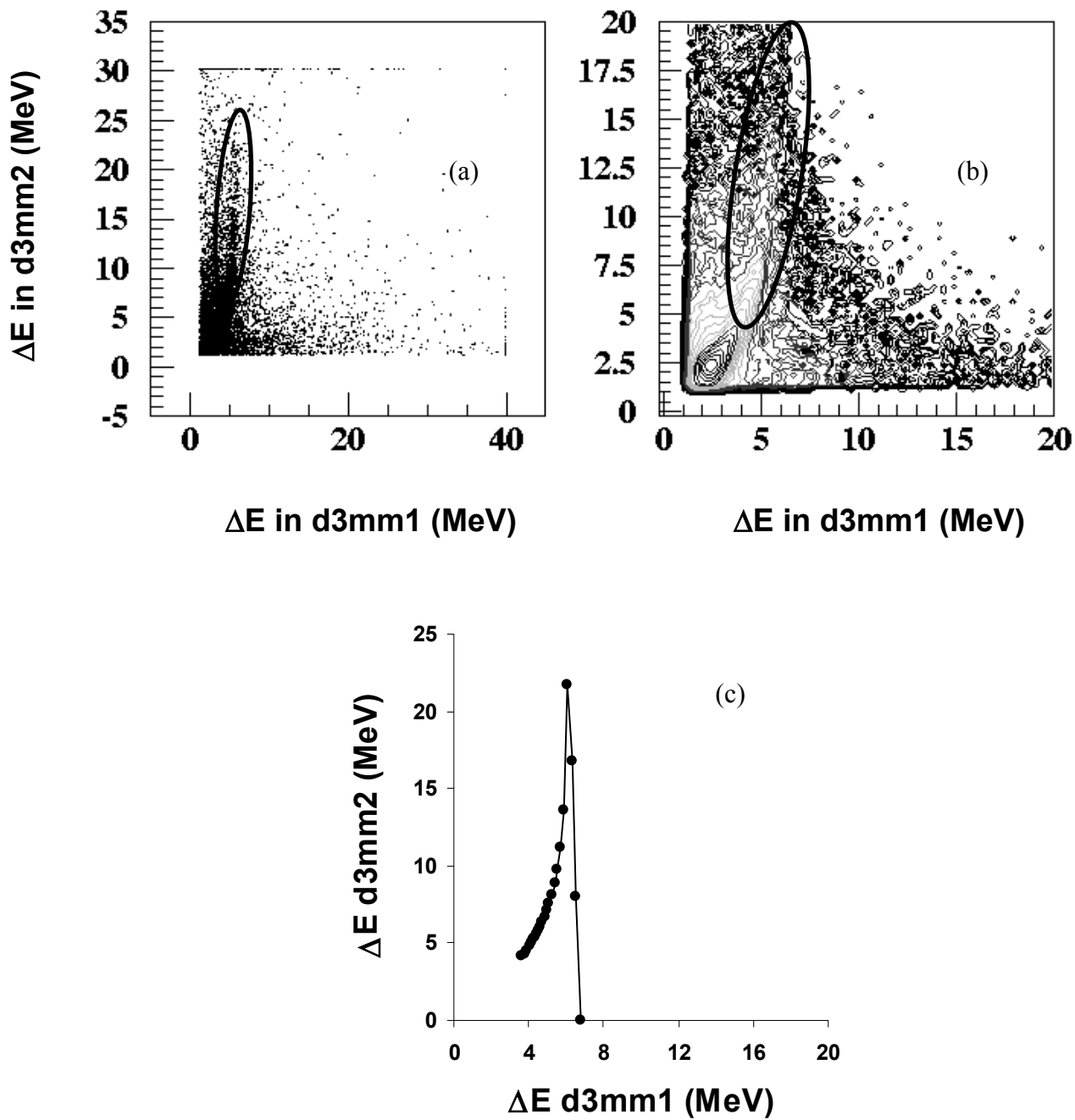
Figure 10. Left: 10(a), scatter plot of ΔE in d3mm2 vs. ΔE in d3mm1 for the run with the detectors in slice 8 of the phantom (upper abdomen). Right: 10(b), same data in the 0-20 MeV range of ΔE, shown as a contour plot. In 10(a) and 10(b), ovals indicate the region populated by slow protons. Bottom: 10(c), calculated ΔE relation accounting only for ionization energy loss.
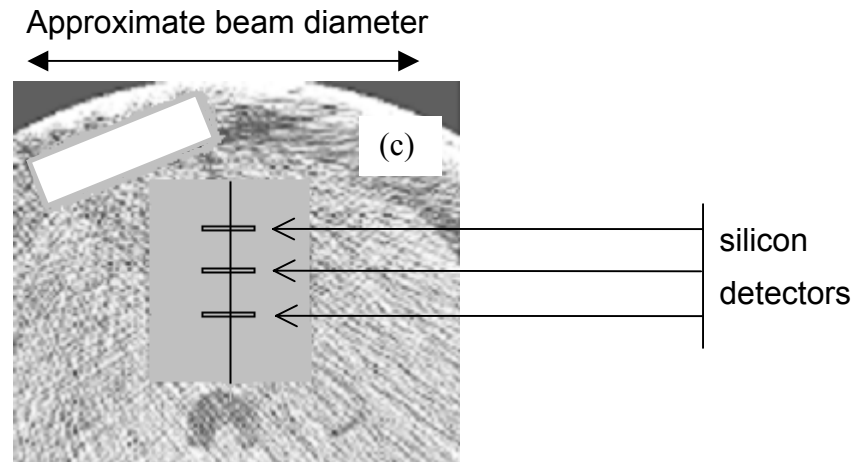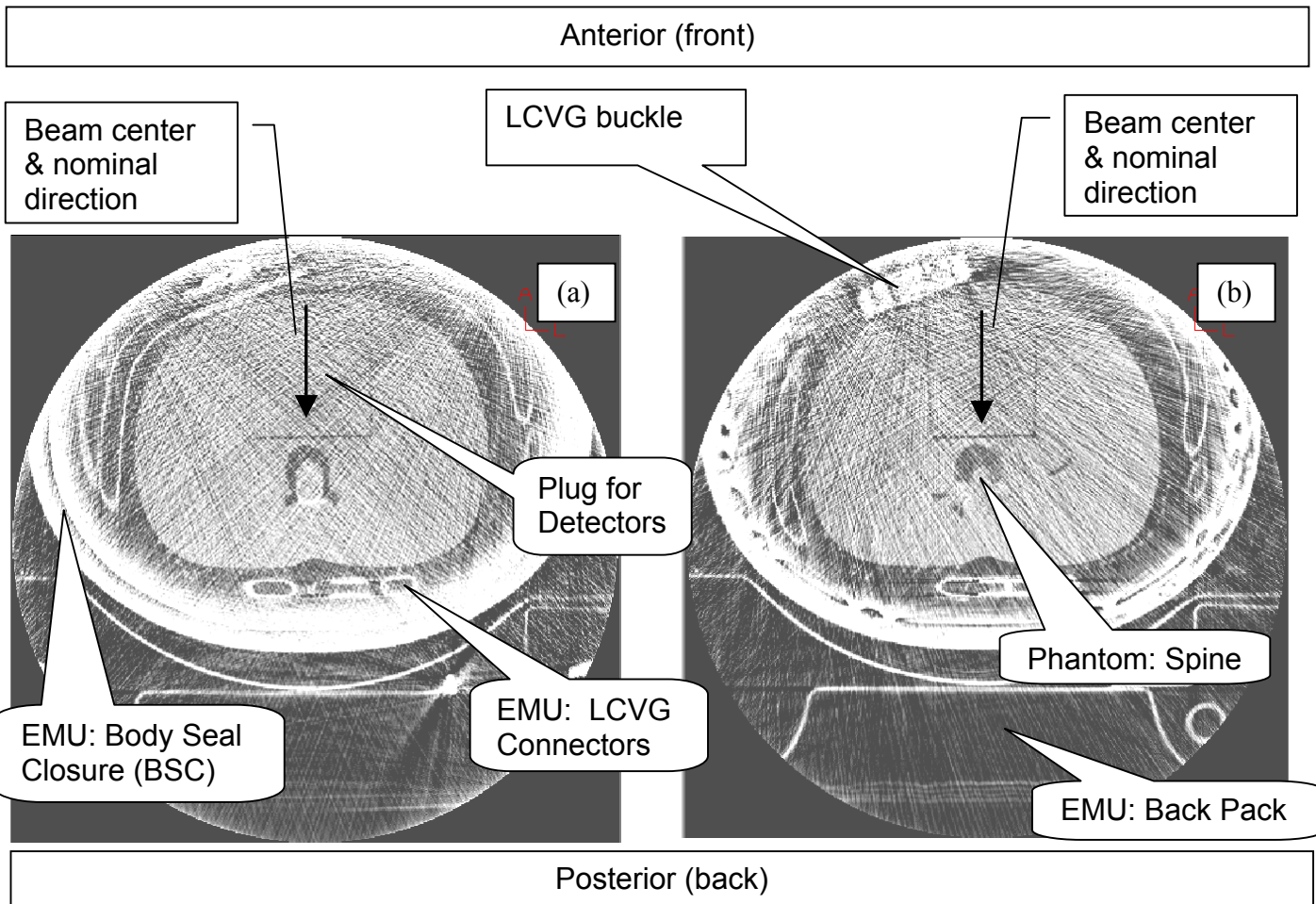
Figure 11. CT images of the spacesuit and phantom, the outline of the Body Seal Closure (BCS) metal joint is shown in 11(a) (upper left). Due to limitations of the CT machine bore and image reconstruction size, only the lower portion of the BCS is visible from these CT images. In 11(b) (upper right), the LCVG buckle can be seen clearly. Fig. 11(c) is centered on the area containing the buckle, detector holder, and detectors.
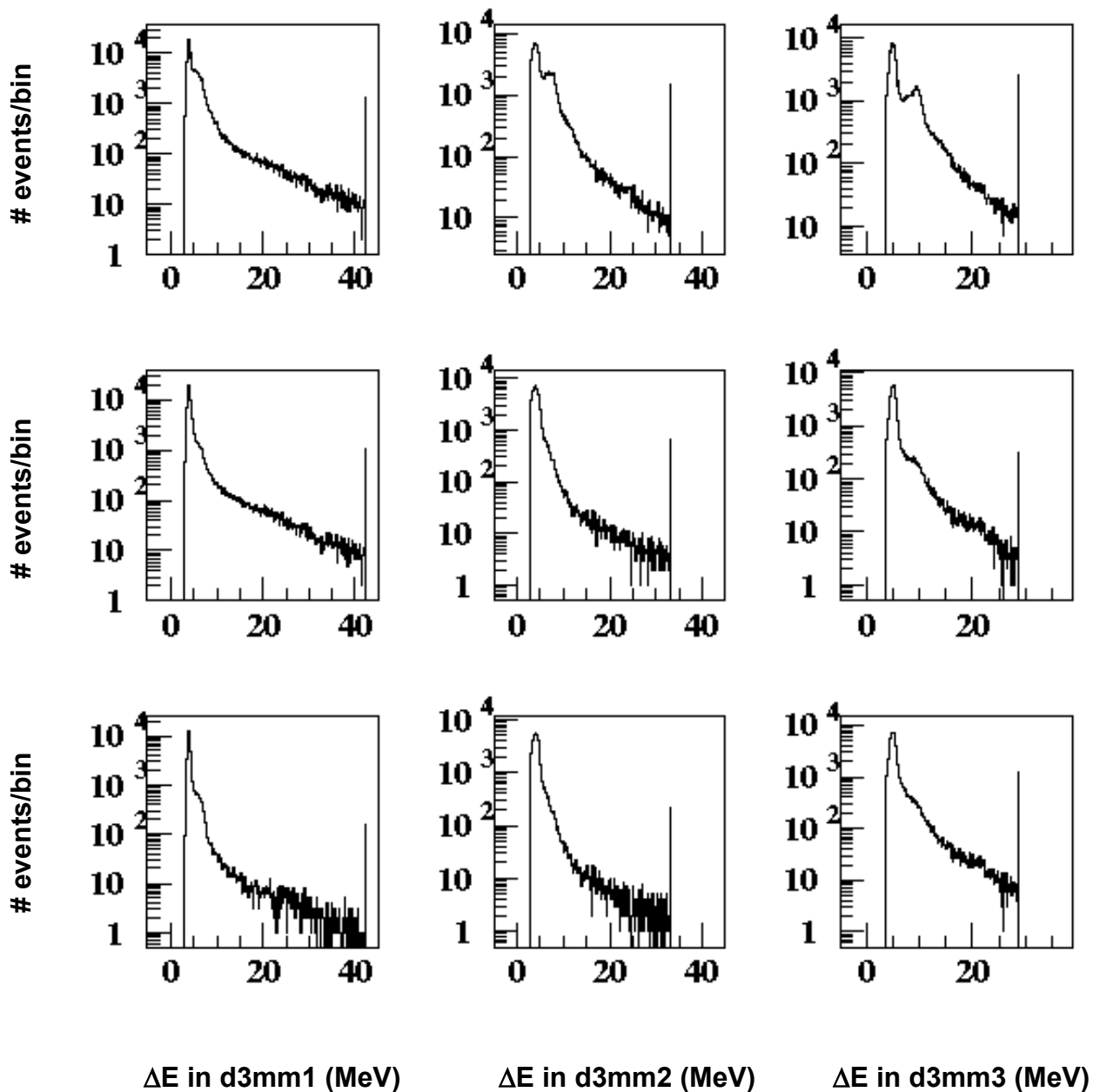
Figure 12. Histograms of ΔE for the run in phantom slice 9 with the 155 MeV extracted beam energy. Top row: Spectra with no cuts to remove pile-up; peaks from 2-proton events are visible, especially in d3mm2 and 3. Middle row: Spectra after method (1) applied. Bottom row: Left-most histogram, d3mm1 after method (3) applied; middle and right, d3mm2 and 3 after method (1) applied.
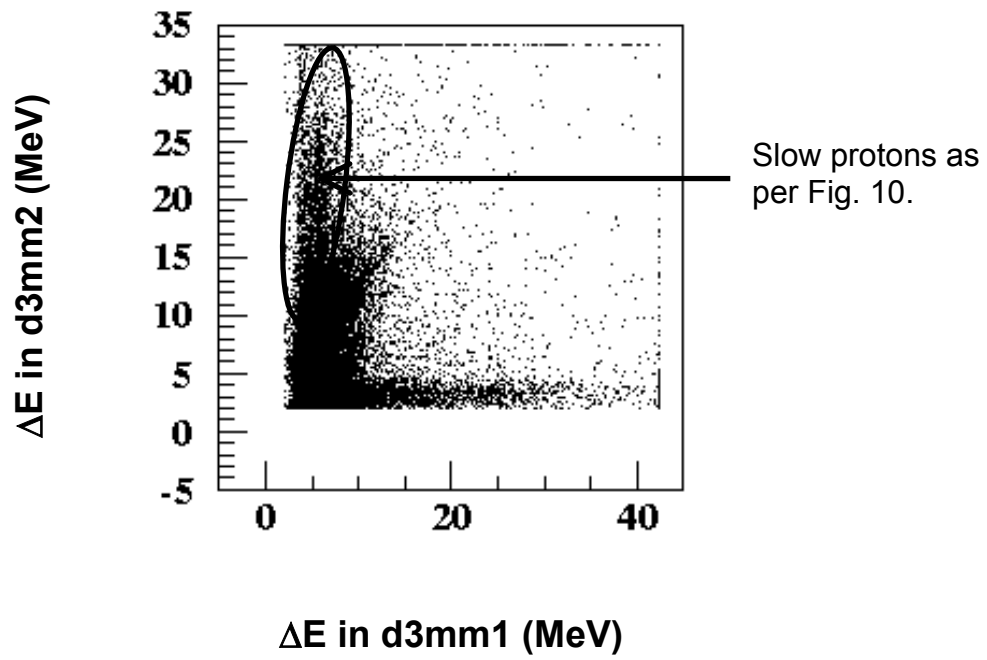
Figure 13. Scatter plot of ΔE in d3mm2 vs. ΔE in d3mm1 for the run with the detectors in slice 9 of the phantom and extracted beam energy of 155 MeV.